Featured in Physics

Mode Interference Effect in Optical Emission of Quantum Dots in Photonic Crystal Cavities

A. Lyasota,[1,2,*] C. Jarlov,[1] M. Nyman,[3] A. Miranda,[1] M. Calic,[1] B. Dwir,[1] A. Rudra,[1] A. Shevchenko,[3] and E. Kapon[1]

[1]*Laboratory of Physics of Nanostructures, Institute of Physics, Ecole Polytechnique Federale de Lausanne (EPFL), CH-1015 Lausanne, Switzerland*

[2]*Centre of Excellence for Quantum Computation and Communication Technology, School of Physics, University of New South Wales, Sydney, New South Wales 2052, Australia*

[3]*Department of Applied Physics, Aalto University, P.O. Box 13500, FI-00076 Aalto, Finland*

(Received 20 October 2021; revised 12 February 2022; accepted 13 April 2022; published 20 May 2022; corrected 22 June 2022 and 12 January 2023)

Radiation properties of a pointlike source of light, such as a molecule or a semiconductor quantum dot, can be tailored by modifying its photonic environment. This phenomenon lies at the core of cavity quantum electrodynamics (CQED). Quantum dots in photonic crystal microcavities have served as a model system for exploring the CQED effects and for the realization of efficient single-photon quantum emitters. Recently, it has been suggested that quantum interference of the exciton recombination paths through the cavity and free-space modes can significantly modify the radiation. In this work, we report an unambiguous experimental observation of this fundamental effect in the emission spectra of site-controlled quantum dots positioned at prescribed locations within a photonic crystal cavity. The observed asymmetry in the polarization-resolved emission spectra strongly depends on the quantum dot position, which is confirmed by both analytical and numerical calculations. We perform quantum interferometry in the near-field zone of the radiation, retrieving the overlap and the position-dependent relative phase between the interfering free-space and cavity-mode-mediated radiative decays. The observed phenomenon is of importance for realization of photonic-crystal light emitters with near unity quantum efficiency. Our results suggest that the full description of light-matter interaction in the framework of CQED requires a modification of the conventional quantum master equation by also considering the radiation mode interference.

DOI: 10.1103/PhysRevX.12.021042 Subject Areas: Optics, Photonics, Quantum Physics

I. INTRODUCTION

Any pointlike source of light changes its properties when placed in a nanoscale optical cavity due to modification of the photonic states into which the source can radiate. A well-known consequence of this is the Purcell effect [1] that reflects the dependence of the photon emission rate on the local density of states (LDOS). While the Purcell effect is a well-studied phenomenon, the influence of the interference of different photonic states on the source emission is much less studied, especially experimentally because of the relatively high technological requirements.

Recently, semiconductor quantum dots (QDs) integrated with photonic crystal (PC) cavities and waveguides have enabled the realization of deterministic single-photon sources with high purity and record brightness [2–7], near unity QD-waveguide coupling efficiency [8,9], and narrow-band emission filters [10], comprising the key elements for on-chip optical information processing and quantum computing. In these schemes, deterministic generation of single photons, e.g., required for optical quantum computing applications [11], is achieved via the adjustment of LDOS. Ideally, increased LDOS enhances the coupling of QD emission to a prescribed mode [1,12] via Purcell's effect and strongly reduces frivolous QD emission into free space [13–16]. The latter comprises radiation losses of QD-PC devices that should be reduced to the level of other losses, e.g., QD nonradiative recombination [17,18] and coupling to the semiconductor matrix [19], via engineering of LDOS of nonconfined modes.

The subwavelength spatial features of the LDOS related to confined states of cavity modes were widely investigated, using various techniques based on single dipole probes, inelastic electron scattering, or scanning near-field optical microscopy (SNOM). In particular, site-controlled Ge QDs [20] and DNA nanoparticles [21] mapped the in-plane LDOS, whereas cathodoluminescence [22] and electron energy-loss microscopy [23] probed the out-of-plane

*Corresponding author.
a.lyasota@unsw.edu.au

LDOS of modes confined in PC cavities. SNOM-based Fano imaging relying on quantum interference between different photon scattering paths displayed the in-plane electric field in PC cavities [24–26] and molecules [27]. Magnetic and electric field components of the cavity modes were probed simultaneously using near-field plasmonic perturbation imaging [28]. The measured near-field profiles qualitatively agree with numerical simulations [20–28]. However, the LDOS of free-space modes (FMs) has remained elusive, as direct QD-free-space emission is typically obscured by the nonradiative decay in time-resolved photoluminescence (PL) traces [29], and the cavity mode electric field mixes with the free-space contribution to LDOS maps obtained in PC cavities [24–26].

In this work, we reveal an important role of the quantum interference between different decay paths of a QD exciton in a PC cavity. These decay paths correspond to the direct and cavity-mode-mediated emission of the QD into free space. The interference exhibits specific spectral features resembling Fano resonances [30]. The strong dependence of the characteristic features of the observed Fano resonances on the location of the QD in the cavity implies the corresponding strong spatial dependence of the QD radiative loss. The latter significantly affects the quantum efficiency of the intracavity QD. Hence, in general, tuning the radiative loss via the QD positioning can be used to improve PC-based quantum sources of light. The observed phenomenon is reproduced using 3D finite element method (FEM) simulations that allowed spanning the large set of design parameters to find essential counterparts affecting the interference. Expanding the concept of Fano imaging [24–27], we perform quantum interferometry of the free-space radiation modes of QD excitons in linear PC cavities using the exciton-cavity mode coupling as a reference. This technique extracts the direct QD free-space radiative decay from the nonradiative recombination, provides access to the near-field profile of the free-space modes, and yields the coupling phases and strengths between the QD exciton and the cavity and free-space modes.

This paper is organized as follows. In Sec. II, we describe our experimental setup and observations that reveal the mode interference phenomenon. In Sec. III, the effects observed in the experiments are demonstrated theoretically. In Sec. IV, we use the experimentally obtained data to retrieve several key characteristics of the QD emission into the relevant spatial modes. Section V characterizes the quantum efficiency of a QD in a PC cavity as a function of the QD position, and Sec. VI summarizes and discusses our observations and the related analysis.

II. EXPERIMENTAL RESULTS

The studied system consists of a single, site-controlled InGaAs/GaAs pyramidal QD positioned at a prescribed location within a modified-L_3 photonic crystal membrane cavity [31–33]. A scanning electron microscope (SEM) image of the cavity is shown in Fig. 1(a) (see also Appendix A, Figs. 7 and 11). Figures 1(b) and 1(c) shows the x- and y-polarized electric field patterns of the fundamental cavity mode (CM) calculated at a half-membrane height. The CM electric field is nearly perfectly y-polarized at the symmetry axis $y = 0$ of L_3 PC cavities [Figs. 1(b) and 1(c)]. In different devices, the ∼20-nm-diameter QDs are placed at nominal distances $\Delta = 0$, 60, 90, 120, or 180 nm from the cavity center [Fig. 1(a) and crosses in Fig. 1(c)], corresponding to different overlaps with the electric field profile of CM. The experimental accuracy of QD positioning is estimated to be better than 10 nm (see Appendix A, Figs. 8–10). The normalized CM near-field amplitude distribution $\Theta_{\mathrm{CM}}(\Delta)$ can be approximated as $\Theta_{\mathrm{CM}}(\Delta) = -e^{-\beta_{\mathrm{CM}}|\Delta|}\cos(2\pi\Delta/\lambda_{\mathrm{CM}})$. Here, the parameter $\beta_{\mathrm{CM}} = 7.9 \times 10^{-4}$ nm^{-1} and the CM effective wavelength $\lambda_{\mathrm{CM}} \approx 340$ nm in the PC cavity defect are obtained by fitting the curve to the 2D finite-difference time-domain (FDTD) CM profile at $y = 0$ [Fig. 1(c)]. The wavelength λ_{CM} corresponds to the effective refractive index $n_{\mathrm{CM}} \approx 2.59$.

Figure 1(d) shows the used microphotoluminescence (μPL) setup. The QDs were optically excited using a Ti:sapphire laser emitting at 730 nm wavelength. The laser beam was focused to a ∼1.5 μm wide spot using a

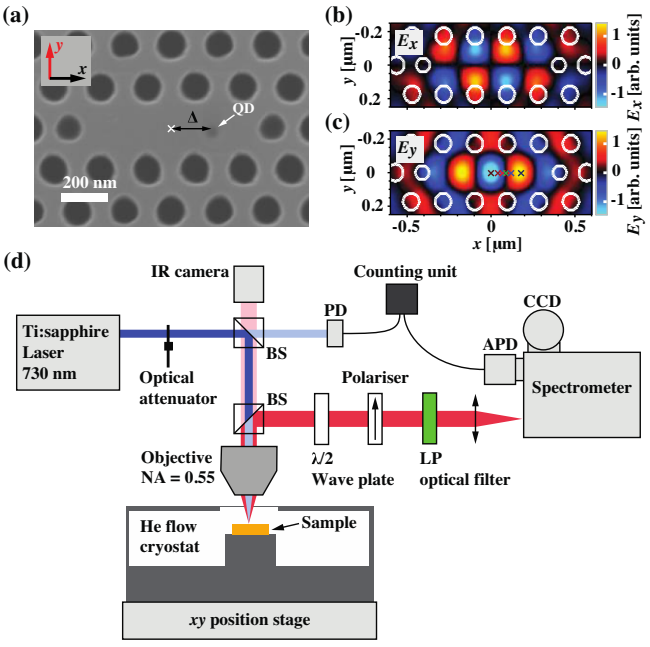

FIG. 1. (a) SEM image of a fabricated structure showing the displacement Δ of the QD from the cavity center. (b),(c) Simulated E_x and E_y electric fields of the fundamental cavity mode at a half-membrane height and 1.42 meV energy. Crosses in (c) show the implemented Δ providing different exciton-CM coupling strengths $g(\Delta)$. The CM near-field patterns in (b) and (c) were calculated using a 2D FDTD method. (d) Schematics of the μPL optical setup. The laser beam used for excitation is highlighted in blue whereas collected photoluminescence is highlighted in red. BS in (d) stands for a nonpolarizing beam splitter.

microscope objective with 50 times magnification, 0.55 numerical aperture, and 3.6 mm working distance. Photoluminescence spectra were measured with the samples placed in a He-flow optical cryostat using the laser in a continuous wave mode and a "Jobin Yvon Triax 550" spectrometer equipped with a charge coupled device (CCD) detector providing a spectral resolution of 80 μeV. The residual excitation light was filtered with a low-pass (LP) optical filter [see Fig. 1(d)]. An infrared camera was used to observe the position of the excitation spot on the sample surface. The x and y coordinates of the spot were controlled with a motorized high-precision (50 nm) xy-position stage. The fine-tuning of the sample position with respect to the excitation spot was achieved by maximizing the QD emission intensity. Time-resolved measurements were carried out using the laser in the mode-locked mode that provided 3 ps laser pulses at 80 MHz repetition rate. A part of the excitation beam was sent to a fast photodiode, serving as a reference for the timing measurements. We used a PicoQuant τ-SPAD-FAST avalanche photodiode (APD) positioned at the monochromator's output. For each spectrally filtered photon arriving at the avalanche photodiode, the time delay from the pump laser pulse was counted by a fast pulse time counting unit (Time Harp 260 TCSPC board, with a 25 ps time bin width).

Polarization-resolved spectra were obtained using a $\lambda/2$ wave plate and a linear polarizer [see Fig. 1(d)]. They were used to calculate the degree of linear polarization (DOLP) given by $D = [(I_y - I_x)/(I_y + I_x)]$, where I_x and I_y are the intensities of the x- and y-polarized components of the emission. The CM was tuned across the QD optical transitions using temperature variations and water vapor condensation [34]. The fundamental mode CM and the next-order mode CM_1 were found to be separated by ~20 meV. The CM quality factor varied from 1500 to 3000 (CM damping rate κ between 0.4 and 1 meV) depending on the device. The QDs emit photons of ~1.42 eV energy at 10 K, with ensemble inhomogeneous broadening of ~10 meV and ~100 μeV wide excitonic transitions.

The polarization-resolved and the corresponding DOLP spectra for a typical structure with QD position $\Delta \approx 0$ are shown in Fig. 2(a). The PL spectra exhibit neutral exciton (X^0), negatively charged exciton (X^-), and biexciton (XX) lines with the energy detuning from the CM depending on the PC hole size and sample temperature. The QD spectrum typically included the contributions from either a negatively or positively charged exciton, a neutral exciton, and a biexcitonic transition that was observed at higher excitation energies. The exciton-CM detuning δ_X of an excitonic complex (X) was defined as its recombination energy E_X relative to the CM energy E_{CM}, $\delta_X = E_X - E_{CM}$. Exciton and CM energies were obtained using Lorentzian fitting of the exciton and CM photoluminescence peaks. For sufficient QD exciton-CM detuning [35,36] (larger than ~10 meV), the cavity mode is not visible in the emission

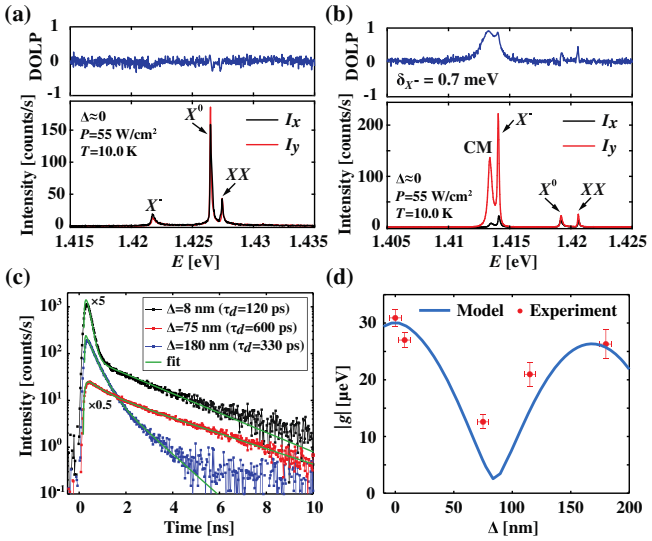

FIG. 2. (a),(b) Polarization-resolved PL (bottom) and corresponding DOLP (top) spectra of excitons emitting inside the photonic band gap and near the resonance with CM. (c) X^- decay traces measured at X^--CM resonance for different Δ. (d) X^--CM coupling strength g versus Δ extracted from the X^- radiative decay rates at the X^--CM resonance.

spectra and the QD emission is coupled to the unpolarized optical modes in the photonic band gap [Fig. 2(a)]. For $\Delta \approx 0$, strong X^--CM overlap near the central CM antinode [see Fig. 1(c)] results in the efficient X^--CM coupling. Hence, for a small exciton-CM detuning [like charged exciton-CM detuning $\delta_{X^-} = 0.7$ meV in Fig. 2(b)], strong X^--CM linear copolarization [29] is evident.

Figure 2(c) shows X^- biexponential decay traces obtained at the X^--CM resonance [29] ($\delta_{X^-} = 0$) for $\Delta = 8$, 75, and 180 nm. The fast X^- decay component in Fig. 2(c), induced by the Purcell's effect, comprises both optical and nonradiative recombination processes [29]. The slow component in the X^- decay traces, corresponding to ~3 ns decay time at $T = 10$ K, is due to QD refilling by carriers captured from charge centers and excitonic bath in the GaAs environment [37]. The equal absolute values of x and y components of the X^- transition dipole [38] directly map the X^- decay rate $\gamma_{X^-} = \tau_d^{-1}$ [Fig. 2(c)] to the CM electric field profile along the symmetry axis at $y = 0$ [Figs. 1(b) and 1(c)]. Figure 2(d) shows the X^--CM coupling strength g as a function of Δ extracted from the X^- decay traces using $\gamma_{X^-} = \gamma_{CM} + \gamma_{FM} + \gamma_{nonrad}$, where $\gamma_{CM} = 4|g|^2/(\kappa + \gamma_d + \gamma_{FM})$ is the on-resonance X^--CM decay rate, γ_{FM} is the rate for the X^- direct decay into free space, and γ_{nonrad}, κ and γ_d are, respectively, the nonradiative decay rate, the CM damping rate, and the X^- dephasing rate [12]. We set $\gamma_{FM} + \gamma_{nonrad} \approx 0.43$ μeV corresponding to the ~1.5 ns X^- decay time obtained from the temperature-dependent X^- dynamics in L_3 PC cavities [29]. The uncertainty on γ_{FM} and γ_{nonrad} rates is insignificant for QDs placed near the CM antinodes. The spatially

resolved X^--CM coupling strength $g(\Delta)$ shown in Fig. 2(d) is in good agreement with a model accounting for the 2D FDTD simulated CM electric field profile, $g(\Delta) = -g_0\Theta_{CM}(\Delta)$, and assuming that $g_0 = 30\ \mu$eV at $\Delta = 0$ [39–41].

Figure 3(a) shows the polarization-resolved emission spectra at positive, zero, and negative detuning of a charged exciton relative to the CM (δ_{X^-}) measured in structures with $\Delta \approx 0$. The spectra are displayed versus the energy E of emitted photons relative to the CM energy, i.e., $E - E_{CM}$. The exciton-CM detuning δ_{X^-} was set by adjusting both temperature and water vapor condensation. We repeatedly observed strongly x-polarized (y-polarized) excitonic transitions at positive (negative) exciton-CM detuning for $\Delta = 0$ leading to an asymmetry in the DOLP spectra. The DOLP asymmetry with respect to zero exciton-CM detuning is clearly visible in the DOLP spectrum shown in Fig. 3(a) for $\delta_{X^-} = -2.1$ meV. This asymmetry is unexpected in the framework of nonoverlapping emission via the CM and directly into free space. In the latter case, the DOLP of the QD transition that has unpolarized emission in the L_3 PC cavity band gap [see Fig. 2(a)] does not drop below 0, as the y-polarized emission via the CM only reduces the total probability of the direct emission into free space and does not affect the near unity ratio of the direct emission probabilities via the x- and y-polarized radiation modes.

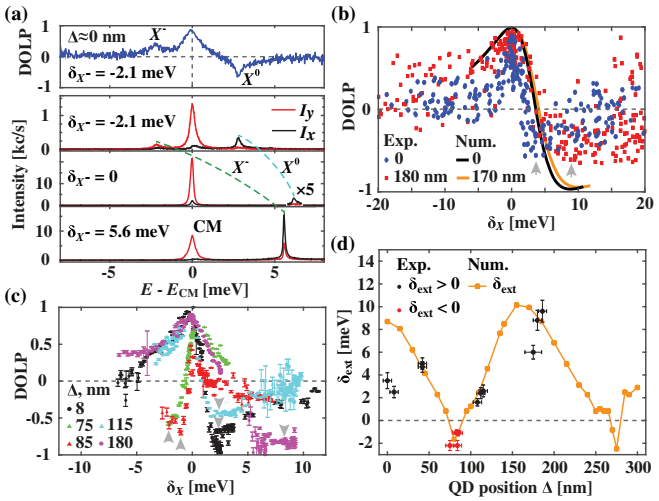

FIG. 3. (a) QD polarization-resolved emission spectra at different X^--CM detunings δ_{X^-} versus the photon energy relative to the CM energy. The bottom and top panels in (a) show the polarized-PL spectra for a structure with $\Delta \approx 0$ and various values of δ_{X^-} and corresponding DOLP for $\delta_{X^-} = -2.1$ meV. The exciton-CM detuning was varied using water vapor deposition and temperature tuning. (b) Numerically simulated DOLP spectra for $\Delta = 0$ and 170 nm and experimental DOLP value statistics versus the exciton-CM detuning. The experimental points were extracted from polarization-resolved PL spectra measured at $P = 170$ W/cm^2 and $T = 10$ K for 61 and 96 different cavities with $\Delta = 0$ and 180 nm, correspondingly. (c) Exciton DOLP values versus the exciton-CM detuning for the QD positions Δ varying from 8 to 180 nm. DOLP traces were obtained by tuning the excitonic transitions across the CM energy as in (a) (see also Appendix A, Fig. 12). (d) Numerically simulated and experimental extremal exciton-CM detuning δ_{ext} extracted from numerical and experimental DOLP traces for different values of Δ. In (b) and (c), δ_X corresponds to the detuning of observed negatively, neutrally, and positively charged excitons and biexcitons relative to the CM energy. Gray arrows mark experimental δ_{ext}.

The negative DOLP at sufficiently large, positive exciton-CM detuning corresponds to a suppressed excitonic emission at the CM polarization. We proved the reproducibility of this phenomenon by probing the DOLP at different exciton-CM detunings in a statistical manner. Multiple spectra were obtained by measuring the exciton emission DOLP in PC cavity arrays incorporating single QDs at $\Delta = 0$, 90, 120, and 180 nm (Appendix A, Fig. 12), while polarization-resolved PL spectra, measured for devices with different PC hole radii, spanned exciton-CM detuning range in the limits of ± 20 meV (see Appendix A, Fig. 13). Figure 3(b) shows the DOLP asymmetry in the statistically yielded emission spectra for structures with $\Delta \approx 0$ and 180 nm superimposed with the DOLP spectra at $\Delta = 0$ and 170 nm numerically simulated using a 3D finite element method (see Appendix B). These DOLP spectra were obtained by modeling the polarization-resolved emission of x- and y-oriented point dipoles in an L_3 PC cavity as a function of the photon energy and the dipole position denoted by Δ (see Appendix B, Figs. 14–16). The observed S-shaped asymmetry in both experimental and numerical DOLP spectra displays predominantly the x-polarized excitonic emission at a positive exciton-CM detuning greater than 3 meV. The best agreement between experimental and 3D FEM DOLP was obtained by accounting for the QD recess (see Appendix B, Fig. 17).

Figure 3(c) shows the S-shaped DOLP curves obtained by tuning the QD optical transitions [as for Fig. 3(a)] across the CM energy in five PC structures, with $\Delta = 8$, 75, 85, 115, and 180 nm, using temperature variation and gas deposition tuning [34]. We were able to tune the excitonic complexes across the energy range wide enough for extracting the extremum exciton-CM detuning δ_{ext} at which the DOLP reaches its lowest negative value corresponding to the maximum exciton-CM cross-polarization [see gray arrows in Figs. 3(b) and 3(c)]. Figure 3(d) shows the experimentally and numerically obtained extremal exciton-CM detuning δ_{ext} taking place at minimum DOLP values. The indicated QD positions Δ were verified using SEM micrographs (see Appendix A, Fig. 10). For all QD positions, except Δ between 70 and 90 nm, experimental δ_{ext} is positive. The dependence $\delta_{ext}(\Delta)$, obtained from the 3D FEM simulated DOLP spectra, is similar to the experimental one. While for almost all values of Δ we find positive δ_{ext}, negative δ_{ext} is observed for Δ ranging from 80 to 85 nm and from 270 to 275 nm (see Appendix B, Fig. 18). Note that the CM has its first and

second node at around $\Delta = 85$ and 255 nm [see Fig. 1(b)] resulting in lower DOLP at the exciton-CM resonance due to smaller CM-QD overlap as visible in Fig. 3(c) for $\Delta = 85$ nm. The observed S-shaped DOLP curves are explained by the Fano-like interference between different QD emission channels in PC cavities [42], as discussed below.

III. THEORETICAL DEMONSTRATION OF THE MODE INTERFERENCE EFFECT IN POLARIZATION-RESOLVED QD EMISSION

Yamaguchi *et al.* theoretically predicted a significant asymmetry in the QD exciton decay rate [43] and emission spectra [42,44] with respect to the zero exciton-CM detuning induced by quantum interference between decay paths through confined cavity modes and nonconfined, free-space modes. The decay rates directly bear on the DOLP asymmetry, as elaborated here by the model schematically illustrated in Fig. 4(a). The exciton is represented by a two-level system (TLS), coupled to a y-polarized CM and x- and y-polarized FMs. Thus, the QD-confined exciton and the fundamental CM considered in this work comprise the classical scheme of two interacting oscillators coupled to the same Markovian bath consisting of FMs [45,46]. Below, the model exciton-CM detuning is denoted by δ_X.

Quantum interference between the direct and cavity-mediated exciton decay paths [Fig. 4(a)] yields a Fano-like resonance that introduces a characteristic asymmetry in

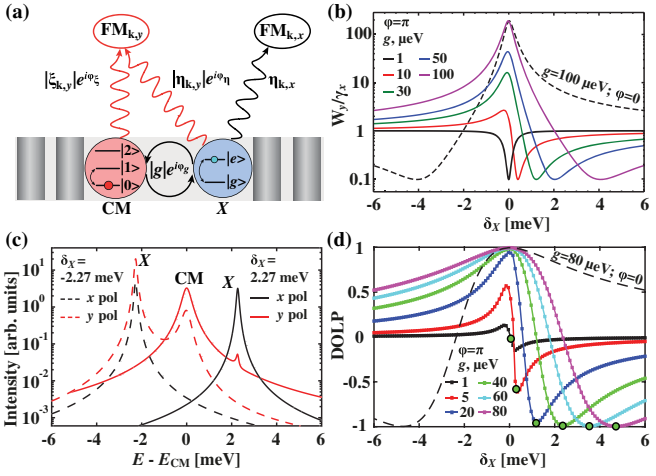

FIG. 4. (a) Schematic representation of radiative FM and CM channels to y- and x-polarized modes. (b) Calculated exciton emission rates $W(\delta_X)$ as a function of exciton-CM detuning δ_X for different exciton-CM coupling strengths g and the phase differences φ. (c) Numerically simulated polarization-resolved spectra for negative and positive detuning δ_X. (d) DOLP traces as a function of δ_X for $p_{\mathrm{CM}} = 0.4$, $p_X = 0.29$, different exciton-CM coupling strengths g, and relative phases φ. The green filled circles represent analytically calculated coordinates $(\delta_{\mathrm{ext}}, D_{\mathrm{ext}})$ of minima in DOLP traces.

the excitonic emission rate $W_y(\delta_X)$ [30,42] through y-polarized FMs with respect to zero exciton-CM detuning δ_X. Allowing for an arbitrary relative phase difference $\varphi = \varphi_g + \varphi_\xi - \varphi_\eta$, the total exciton emission rate into the y-polarized FMs is given by

$$W_y(\delta_X) = \frac{\kappa + \gamma_y}{2} - \mathrm{Re}\left[\left(\frac{\kappa - \gamma_y}{2} - i\delta_X\right)^2 - (2|g| - i\chi\sqrt{\gamma_y\kappa}e^{-i\varphi}) \times (2|g| - i\chi\sqrt{\gamma_y k}e^{i\varphi})\right]^{1/2}, \quad (1)$$

χ is the 3D overlap of the direct and CM-mediated radiation patterns [30,42] (see Appendixes C 1 and C 2). Figure 4(b) shows the computed ratio $W_y(\delta_X)/\gamma_x$, where γ_x is the decay rate into x-polarized FMs, for different exciton-CM coupling strengths. Destructive mode interference is manifested by the reduction in the emission rate $W_y(\delta_X)$ resulting in $W_y(\delta_X) \ll \gamma_x$ for positive exciton-CM detuning δ_X with $\varphi = \pi$ [Fig. 4(b)]. The total exciton emission rate $W_y(\delta_X)$ through y-polarized FMs is significantly higher than the emission rate through x-polarized FMs (γ_x) at negative detuning δ_X due to constructive interference of the FM- and CM-mediated decays through y-polarized modes. The observed effect is sensitive to the relative phase φ: the emission rates are reduced for negative (positive) detuning when $\varphi = 0$ ($\varphi = \pi$).

We took into account the QD exciton dephasing by numerically solving the quantum master equation (QME) that included the interference between the overlapping FM- and CM-mediated decays into y-polarized modes. The interactions among the exciton, CM, and FMs are formulated within the Jaynes-Cummings Hamiltonian [47] (see Appendix C 3) using complex coupling strengths $g = |g|e^{i\varphi_g}$ (for X-CM coupling), $\xi_{\mathbf{k},y} = |\xi_{\mathbf{k},y}|e^{i\varphi_\xi}$ (CM-FM coupling), $\eta_{\mathbf{k},y} = |\eta_{\mathbf{k},y}|e^{i\varphi_\eta}$ (X-FM coupling), and $\eta_{\mathbf{k},x}$ (X-FM coupling), where $\mathbf{k}$ stands for the FM wave vector. We assumed $|\eta_{\mathbf{k},x}| = |\eta_{\mathbf{k},y}|$ ensuring isotropic (equal) radiative decay rates through the x- and y-polarized FMs. Coupling between CMs and x-polarized FMs is neglected and the X-FM and CM-FM coupling phases φ_η and φ_ξ are assumed to be independent of the wave vector $\mathbf{k}$. The CM and X damping rates were assumed independent of the photon energy. We set phases $\varphi_g = 0$ and $\varphi_\eta = 0$ at $\Delta = 0$ for the negative y component of CM and FM electric fields and the positive y component of the transition dipole moment at the center of the cavity [48]. We assume the same form of the normalized spatial profile $\Theta_{\mathrm{FM}}(\Delta)$ for all nonconfined modes, i.e., $\eta_{\mathbf{k},p}(\Delta) = -\eta_{\mathbf{k},p}(0)\Theta_{\mathrm{FM}}(\Delta)$, where $p = \{x, y\}$. Also, we restrict our analysis to real values of $\Theta_{\mathrm{FM}}(\Delta)$.

The response of the experimental setup to the emitted light was taken into account using the 3D FDTD simulated collection efficiencies p_{FM} and p_{CM} of the FM- and CM-mediated excitonic emission [49]. Figure 4(c) shows

the numerically computed polarization-resolved spectra for negative and positive X-CM detuning δ_X, exciton dephasing rate $\gamma_d = 60$ μeV, phase $\varphi = \pi$, and emission overlap within the objective lens aperture $\chi_A = 1$ [49]. Destructive interference between different exciton decay channels into the y-polarized FMs results in nearly complete suppression of y-polarized exciton emission at $\delta_X = 2.27$ meV [Fig. 4(c)]. The latter leads to the cross-polarized X-CM emission at positive exciton-CM detuning, closely capturing the behavior observed in the experimental polarization-resolved spectra [Fig. 3(a)].

Figure 4(d) displays DOLP spectra extracted from the numerically simulated polarization-resolved spectra as in Fig. 4(c) for several values of the X-CM coupling strength g at $\varphi = 0$ or π. Whereas a clear X-CM copolarization (DOLP ≈ 1) occurs for sufficiently small detuning δ_X due to Purcell enhancement, the negative DOLP values represent the X-CM cross-polarization, for certain positive (negative) detuning if $\varphi = \pi$ ($\varphi = 0$). The extremal detuning δ_{ext} and the DOLP minimum value D_{ext} can be obtained analytically in the Weisskopf-Wigner approximation in the limit of $|\delta_{\text{ext}}| \gg \gamma_d$ (see Appendix C 2) as

$$\delta_{\text{ext}} = \frac{g(p_{\text{FM}}^2\gamma_y - p_{\text{CM}}^2\kappa)}{p_{\text{FM}}p_{\text{CM}}\sqrt{\kappa\gamma_y}\chi_A\cos\varphi}, \tag{2}$$

$$D_{\text{ext}} = \left[1\text{–}2\left(\frac{1+\gamma_d^2/\delta_{\text{ext}}^2}{\chi_A\cos\varphi}\right)^2\right]^{-1}, \tag{3}$$

where κ is the CM damping rate. This analytical approximation agrees well with the numerically modeled DOLP spectra [see green circles in Fig. 4(d) and in Appendix B, Figs. 18 and 19].

IV. SPATIAL MAPPING OF THE QD DIRECT EMISSION RATE γ_{FM}, RELATIVE PHASE φ, AND OVERLAP χ_A

The values of δ_{ext} and D_{ext}, extracted from experimental DOLP traces, permit retrieving the overlap χ_A, the relative phase φ, and the direct excitonic emission rate $\gamma_{\text{FM}} = \gamma_x + \gamma_y$ through both x- and y-polarized nonconfined modes given by

$$\chi_A\cos\varphi = \frac{(1+\gamma_d^2/\delta_{\text{ext}}^2)\delta_{\text{ext}}}{|\delta_{\text{ext}}|}\sqrt{\frac{2D_{\text{ext}}}{D_{\text{ext}}-1}}, \tag{4}$$

$$\gamma_{\text{FM}} \approx \frac{2\kappa p_{\text{CM}}^2 g^2}{(\delta_{\text{ext}}p_{\text{FM}}\chi_A\cos\varphi)^2}, \tag{5}$$

as derived from Eqs. (2) and (3) for $\gamma_y \ll \kappa$. Figure 5(a) shows the direct X^--FM emission rate $\gamma_{\text{FM}}(\Delta)$ into free space obtained from measured $\delta_{\text{ext}}(\Delta)$ [Fig. 3(d)] and the X-CM coupling strength $g(\Delta)$ [Fig. 2(d)]. The relative FM LDOS in Fig. 5(a) is given by $[\rho_{\text{FM}}(\Delta)/(\rho_{\text{bulk}})] = [\gamma(\Delta)/\gamma_{\text{bulk}}]$, where ρ_{bulk} is the FM LDOS in bulk GaAs and the X^- emission rate $\gamma_{\text{bulk}} \approx 0.43$ μeV corresponds to the observed $\sim$1.5 ns X^- decay time in bulk GaAs [50] at $T = 10$ K. The X^- emission rate and the corresponding FM LDOS [Fig. 5(a)] are strongly modulated revealing an order of magnitude difference between $\Delta \approx 0$ and 80 nm. Such spatial modulation in the FM LDOS is particularly significant in membrane PCs, as previously observed in both experiments [22] and simulations [51]. The span of $\rho_{\text{FM}}(\Delta)/\rho_{\text{bulk}}$ in Fig. 5(a) is comparable with the depth of the band gap in membrane PCs at different positions of the dipole emitter [18,51] and consistent with previously observed inhibition of the excitonic emission rate in PC nanocavities [13,14].

Figure 5(b) shows the relative phase φ and CM-FM overlap χ extracted from the measured δ_{ext} and D_{ext}. The negative and positive extremal detuning δ_{ext} in Fig. 3(d) gives $\varphi \approx 0$ for $70 < \Delta < 90$ nm and $\varphi \approx \pi$ for $\Delta < 60$ nm or $\Delta > 90$ nm resulting in two phase jumps by π at $\sim$70 and $\sim$90 nm [Fig. 3(d)]. The observed phase shift at $\Delta \approx 85$ nm is explained by opposite signs of the y component of the CM electric field at different sides of the CM node at $y = 0$; that is, for $\Delta < 90$ nm and $\Delta > 90$ nm [Fig. 1(c)]. The change of the relative phase by π near $\Delta \approx 70$ nm [Fig. 5(b)] defines the node position of the near-field profile of nonconfined modes as also manifested by the reduced FM LDOS [Fig. 5(a)]. The CM-FM coupling phase φ_ξ is equal to the relative phase φ at $\Delta = 0$ [Fig. 5(b)]; that is, $\varphi_\xi \approx \pi$ for $\varphi_g = 0$ and $\varphi_\eta = 0$.

Taking into account that the excitonic emission rate through nonconfined modes $\gamma_{\text{FM}}(\Delta) = [(2\pi)/\hbar] \times \sum_{\mathbf{k},p=\{x,y\}} \eta_{\mathbf{k},p}(\Delta)\eta^*_{\mathbf{k},p}(\Delta)$, we obtain $\gamma_{\text{FM}}(\Delta) = \gamma_{\text{FM}}(0) \times \Theta^2_{\text{FM}}(\Delta)$ and $|\Theta_{\text{FM}}(\Delta)| = \sqrt{\rho_{\text{FM}}(\Delta)/\rho_{\text{FM}}(0)}$, while $\arg[\Theta_{\text{FM}}(\Delta)] = \varphi_\eta(\Delta) = \varphi_g(\Delta) + \varphi_\xi - \varphi(\Delta)$. The exciton-CM coupling phase φ_g is either 0 or π leading to $\Theta_{\text{FM}}(\Delta) = \Theta_{\text{CM}}(\Delta)\sqrt{\rho_{\text{FM}}(\Delta)}\cos[\varphi(\Delta) - \varphi_\xi]/[|\Theta_{\text{CM}}(\Delta)|\sqrt{\rho_{\text{FM}}(0)}]$. Figure 5(c) shows the FM spatial profile thus extracted from the FM LDOS $\rho_{\text{FM}}(\Delta)$ and the relative phase $\varphi(\Delta)$ shown in Figs. 5(a) and 5(b). The modeled excitonic emission rate through nonconfined modes, $\gamma_{\text{FM}}(\Delta) = \gamma_0\Theta^2_{\text{FM}}(\Delta)$, where $\gamma_0 = 0.236$ μeV, is in good agreement with the experimental results [see Fig. 5(a)]. Discontinuity in the experimental $\delta_{\text{ext}}(\Delta)$, observed for $\Delta \approx 70$ nm [see Fig. 3(d)], additionally points toward the y-polarized FM node positions, since $\delta_{\text{ext}}(\Delta) \sim 1/\Theta_{\text{FM}}(\Delta)$. In contrast, $\delta_{\text{ext}}(\Delta) \sim \Theta_{\text{CM}}(\Delta)$ and approaches zero at the CM node $\Delta \approx 90$ nm. Here, we modeled the FM normalized spatial profile using the same form as for $\Theta_{\text{CM}}(\Delta)$, i.e., $\Theta_{\text{FM}}(\Delta) = -e^{-\beta_{\text{FM}}|\Delta|}\cos[(2\pi\Delta)/(\lambda_{\text{FM}})]$, where $\beta_{\text{FM}} = 3.6 \times 10^{-4}$ nm^{-1} and $\lambda_{\text{FM}} = 266$ nm. The effective wavelength λ_{FM} approximately corresponds to the effective refractive index $n_{\text{FM}} = 3.27$, close to the mode index of a 250-nm-wide GaAs slab [52].

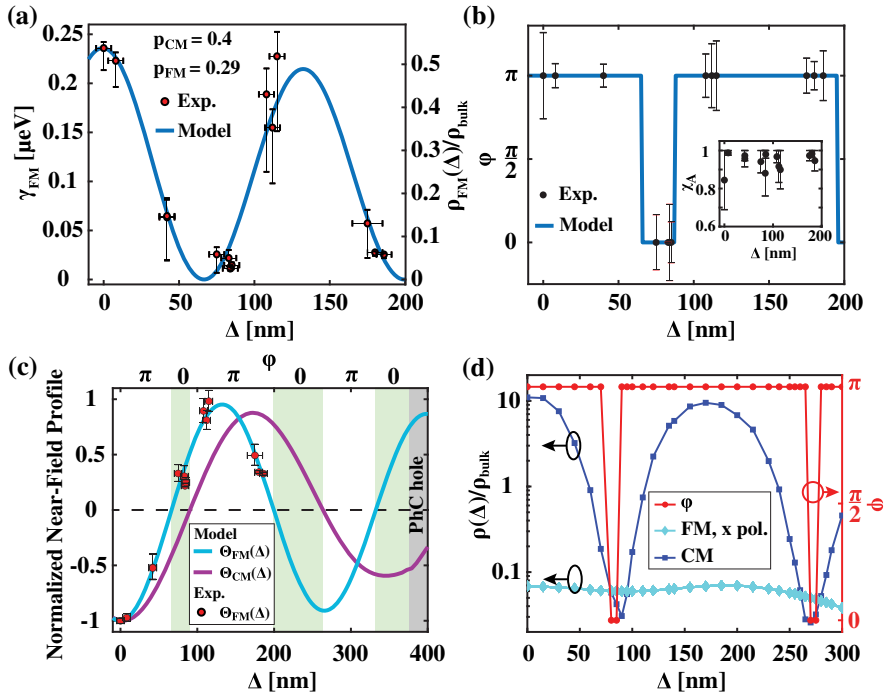

FIG. 5. (a) Direct X^--FM emission rate $\gamma_{FM}(\Delta)$ and the corresponding LDOS $\rho_{FM}(\Delta)$ in units of homogeneous LDOS in bulk GaAs (right-hand ordinate). Spatial dependences of the experimental $\rho_{FM}(\Delta)$ and relative phase φ are matched by the model based on the mapped FM spatial profile. (b) The extracted relative phase φ. The CM-FM overlap χ_A is shown in the inset as a function of QD position Δ. (c) Normalized electric field profile of free-space modes at half-membrane height reconstructed from the extracted $\rho_{FM}(\Delta)$ in (a) and the relative phase $\varphi(\Delta)$ in (b). The CM profile, extracted from the 2D FDTD simulations in Fig. 1(c), is shown for reference. Green and white areas in (c) correspond to $\varphi = 0$ and π, respectively. Gray region denotes a side view of the PC hole [see Fig. 1(a)]. (d) Relative phase φ, CM, and x-polarized FM LDOS $\rho(\Delta)$ relative to the bulk LDOS as a function of Δ calculated using 3D FEM.

Thus, the X-CM and X-FM coupling phases are given by $\varphi_g(\Delta) = \pi - \arccos[\Theta_{CM}(\Delta)/|\Theta_{CM}(\Delta)|]$ and $\varphi_\eta(\Delta) = \pi - \arccos[\Theta_{FM}(\Delta)/|\Theta_{FM}(\Delta)|]$. We explain the observed CM-FM coupling phase φ_ξ by the mutual orientation of CM and FM electric fields at the side holes of the PC cavity [$|y| \approx 375$ nm in Figs. 1(c) and 5(c)] playing the major role in the radiative CM coupling to free space [53]. Therefore, φ_ξ can be modeled as $\varphi_\xi = \arccos[\Theta_{CM}(L)\Theta_{FM}(L)|\Theta_{CM}(L)\Theta_{FM}(L)|^{-1}]$, where $L = 375$ nm. The resulting relative phase $\varphi(\Delta) = \varphi_g(\Delta) + \varphi_\xi - \varphi_\eta(\Delta)$ agrees well with the experiments [see the blue line in Fig. 5(b)].

Figure 5(d) shows the relative phase φ, CM, and x-polarized FM LDOS simulated using 3D FEM for discrete values of Δ spanning from 0 to 300 nm. The positions of the CM LDOS maxima, spaced by ~170 nm, correspond to the maxima in the CM near-field profile [CM characteristic wavelength is $\lambda_{CM} \sim 340$ nm; see Figs. 1(c) and 5(c)]. The x-polarized FM LDOS also shows an oscillatory behavior with a period of about 190 nm corresponding to $\lambda_{FM} \sim 380$ nm (see also Appendix B, Fig. 14). The observed phase shifts in Fig. 5(d) are of the same nature as the phase shifts observed in the experiments [Fig. 5(b)], i.e., caused by the difference in the node positions of CM and FM profiles. Quantitatively, the second phase jump takes place at a larger value of Δ than in the experiments. We explain this difference by a much smaller number of PC hole rows used in 3D FEM simulations that alters nodes' locations of the FM LDOS. It should be noted that the QD recess strongly affects the relative phase φ as observed in 3D FEM simulations (see Appendix B, Fig. 17). Therefore, the experimentally observed FM profiles include the impact of the residual QD recess.

Precise knowledge of the FM near-field profile paves the way for engineering QD-PC devices with improved functionality via control of direct and CM-mediated decay channels. In particular, the second CM antinode is close to the second FM node [Fig. 5(c)] due to significant difference between CM and FM effective refractive indices ($n_{CM} \approx 2.59$ and $n_{FM} \approx 3.27$). QDs placed near FM nodes at $\Delta = 65$ and 200 nm have a vanishing radiative coupling to FMs, but significant QD-CM overlaps (40% and 70%). Thus, QD-PHC devices with near unity quantum efficiency can be engineered via optimization of the $\gamma_{FM}(\Delta)/\gamma_{CM}(\Delta)$ ratio using the QD position Δ as a tuning parameter.

V. QUANTUM EFFICIENCY OF A SINGLE QUANTUM DOT IN A PHOTONIC-CRYSTAL CAVITY

Figure 6 shows the quantum efficiency [12,54] of a charged exciton X^- in a PC cavity, $QE = \gamma_{CM}(\Delta)/[\gamma_{CM}(\Delta) + \gamma_{FM}(\Delta) + \gamma_{nonrad}]$, as a function of QD position

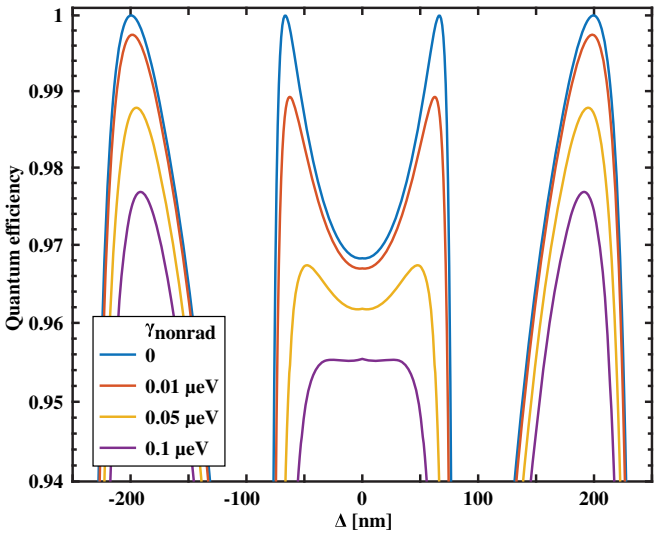

FIG. 6. Quantum efficiency of a QD in a PC cavity as a function of Δ, simulated for a set of nonradiative decay rates γ_{nonrad}.

Δ modeled in a bad cavity regime $g \ll \kappa/4$. Here, γ_{nonrad} is the X^- nonradiative decay rate, $\gamma_{\mathrm{CM}}(\Delta) = 4|g(\Delta)|^2/[\kappa + \gamma_d + \gamma_{\mathrm{FM}}(\Delta)]$ is the X^- emission rate at the X^--CM resonance, CM damping rate is $\kappa = 400$ μeV, and X^- dephasing rate is $\gamma_d = 100$ μeV. The function $\gamma_{\mathrm{FM}}(\Delta)$ and $g(\Delta)$ were assumed to be the same as in Figs. 2(d) and 5(a).

The modeled quantum efficiency strongly varies with Δ due to both spatial dependence of the QD direct and CM-mediated emission rates. QDs placed at $\Delta = 65$ and 200 nm have a vanishing radiative coupling to FMs, but significant QD-CM overlaps (40% and 70%) [see Figs. 1(c), 2(d), and 5(a)]. As a result, the Purcell enhancement is only 2 times weaker at $|\Delta| = 200$ nm than at $\Delta = 0$ prior to at least 70% QD-CM overlap. The resulting maximum QE at $|\Delta| = 200$ nm exceeds the values of QE at $\Delta = 0$ for realistic nonradiative losses $\gamma_{\mathrm{nonrad}} < 0.1$ μeV (~6 ns nonradiative decay time) [17,18] and can reach a value close to 1. Therefore, the spatial dependence of the QD exciton direct radiative decay in L_3 PC cavities opens a novel pathway for optimizing the quantum efficiency of the PC-cavity-based single-photon emitters.

VI. DISCUSSION

Our results constitute the first experimental demonstration of quantum interference between overlapping direct and CM-mediated dissipation channels of QD excitons in photonic cavities. The latter leads to a strong exciton-CM cross-polarization effect that well agrees with the predicted interference effect in emission spectra of solid-state emitters in photonic cavities [42]. Commonly used approaches ignore the interference of overlapping dissipation channels and fail to describe the related phenomena, among which are the cross-polarization effect, asymmetry in vacuum Rabi spectra [42,49], as well as Fano effect in decay rates [30,42] and emission [42] spectra. Our results show that the full description of light-matter interaction in the framework of cavity quantum electrodynamics requires modification of the QME approaches by introducing the cross-term Liouville superoperator [42] or calculating the cross-term contribution in the power spectrum [49] (see Appendix C 3).

Our observations verify the key assumptions in the derivation of the Markovian QME approach accounting for the quantum interference: (1) the coupling constants $\xi_{\mathbf{k},y}$ and $\eta_{\mathbf{k},y}$ can be written as $\xi_{\mathbf{k},y} \cong \xi(\omega)$ and $\eta_{\mathbf{k},y} \cong \eta(\omega)$, and (2) $\xi(\omega)$, $\eta(\omega)$, and the density of states of the continuum $D(\omega) \equiv \sum_{\mathbf{k}} \delta(\omega - \omega_{\mathbf{k}})$ are smooth function of ω [42]. The assumption (1) corresponds to the phases φ_ξ and φ_η independent of the wave vector $\mathbf{k}$ as was suggested above. As a result, the resonant feature in the spectrum is not averaged over the wave vectors and a clear relative phase φ can be extracted from the experimental data. The assumption (2) is confirmed by the great conformity of the numerically calculated and experimental DOLP spectra [see Figs. 3(b), 3(c), and 4(d)]. Moreover, our results show nearly unity overlap χ_A within the objective aperture [Fig. 5(b)]. We expect that the total overlap χ between direct and CM-mediated decay channels is very close to the calculated χ_A.

Quantum interferometry, based on mapping of interference features with site-controlled QDs, allows probing both phase and amplitude of the near-field pattern of free-space modes in the PC cavity. FM LDOS had pronounced minima, which can be fruitful for designing QD-PC single-photon sources with improved quantum efficiency. Analysis of the spatially resolved relative phase φ between the direct FM and CM-mediated emission channels revealed the CM-FM coupling phase $\varphi_\xi = \pi$, characteristic to the PC cavity design. Remarkably, experimental observations well agree with the 3D FEM simulations highlighting the strength of the method for studying light-matter interaction in photonic devices.

ACKNOWLEDGMENTS

This work was supported by Swiss National Science Foundation and Academy of Finland (Grant No. 308394). This research was funded by the Swiss National Science Foundation Grant No. 200021_169514, Integrated Quantum Photonics for Single-Photon Manipulation and High Bandwidth Optical Communication (I-QUANTPHOT).

APPENDIX A: EXPERIMENTS

1. Alignment between QD and PC cavity arrays

The InGaAs/GaAs QDs are self-formed during metal-organic vapor phase epitaxy in pyramidal recesses etched on (111)B GaAs/AlGaAs/GaAs substrates [31–33] and their nucleation site is fixed with an accuracy of ~10 nm using electron beam lithography [see Figs. 7–10). The modified L_3 cavities consisted of three missing holes in a triangular array of holes (pitch $a = 200$ nm) etched in a

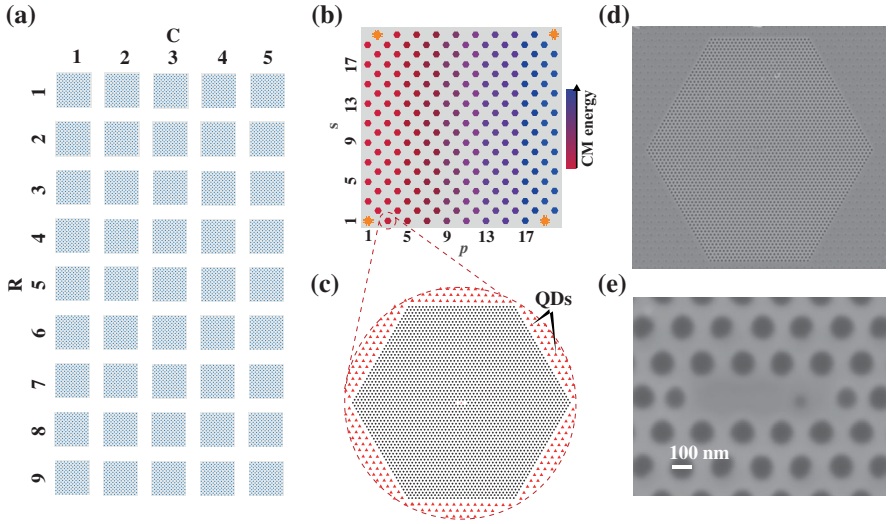

FIG. 7. Sample design. (a) An arrangement of 45 square arrays of PC cavities in 9 rows with 5 columns. (b) An arrangement of 200 PC cavities in a single array. (c),(d) A sketch and a SEM micrograph of an L_3 PC cavity integrated with a single QD. (e) SEM of a PC cavity with a visible QD position. Sacrificial QDs arranged in a triangular lattice with a period twice that of the PC hole lattice are removed by the PC cavity holes as visible in (d).

~250 nm GaAs suspended membrane layer. The QD and PC hole patterns were fabricated using electron beam lithography with relative alignment accuracy of ~10 nm. For each value of the QD position Δ, the radius of the PC holes was varied systematically to scan the cavity mode energy across the QD spectrum [35]. Each group of devices with the same Δ was repeated in 5 PC cavity arrays consisting of 200 devices with 10 different PC hole radii (see Fig. 7) allowing the CM energy tuning across the QD emission lines (see Fig. 11).

The investigated sample contained 45 PC cavity arrays, each composed of 200 cavities, that were arranged in 9 rows with 5 columns [Figs. 7(a) and 7(b)]. Rows with numbers 2, 3, 4, 7, and 8 had PC cavities incorporating single QDs with nominal $\Delta = 180$, 120, 90, 60, and 0 nm, correspondingly. Other rows contained L_3 PC cavities with 2 QDs or L_7 PC cavities with 2, 3, or 4 QDs. In each square array, the fundamental and the first excited CM resonance energies were tuned across the expected QD emission energy measured prior to fabrication of PC cavities by increasing PC hole radii with the PC cavity number p. Devices were referenced via square array row number (R), column number (C), series number (s), and PC cavity number (p) [Figs. 7(a) and 7(b)]. Figures 7(d) and 7(e) show SEM micrographs obtained for the device "R2C3s7p6} using small and large magnifications.

We repeatedly achieved QD-PC cavity alignment accuracy of better than 10 nm [55] as shown in Fig. 8.

Within a square array, x- and y-misalignment errors varied in the limits of about 10 nm as shown in Fig. 9. Each array was aligned independently with a unique set of alignment marks. It should be noted that these variations

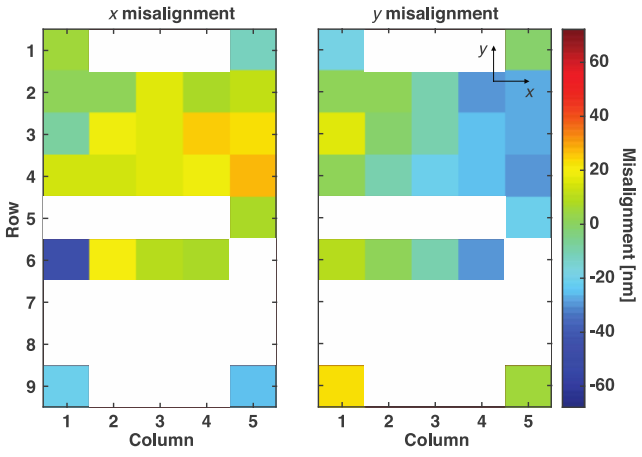

FIG. 8. QD-L_3 PC cavity alignment accuracy. The x- and y-misalignment errors measured for the corner devices of several square arrays.

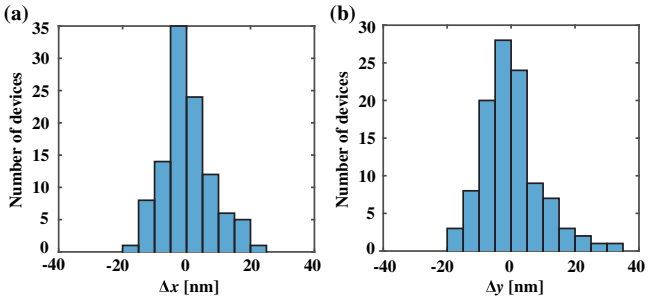

FIG. 9. QD-PC cavity alignment fluctuations within several square arrays. (a),(b) Histograms of x and y alignment deviations from Δ mean values calculated from alignment data measured in several PC cavities in each array (data from 14 different arrays, several devices per array).

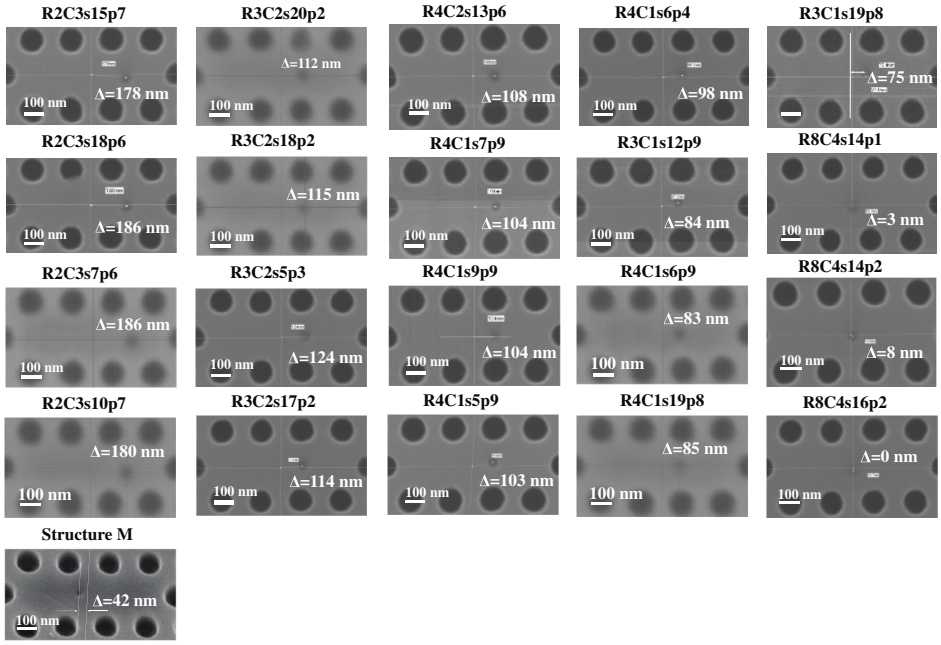

FIG. 10. Determination of the QD-PC cavity alignment accuracy using SEM. SEM images of GaAs/InGaAs pyramidal QDs with prescribed positions in a modified L_3 PC membrane cavity.

are mainly caused by the measurement error of the QD recesses position.

Figure 10 shows SEM micrographs of several structures with the measured QD position Δ. It should be noted that DOLP data for $\Delta = 42$ nm (SEM micrograph of structure M) was previously reported in Refs. [35,56]. DOLP for the structure with $\Delta = 175$ nm (not shown here) was reported in Refs. [36,56].

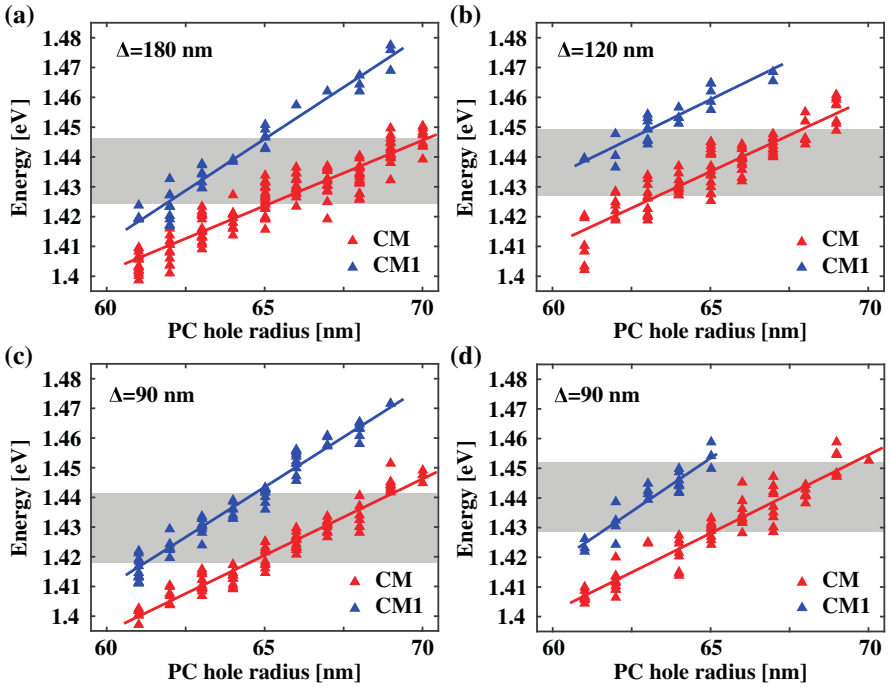

FIG. 11. Fundamental and the first excited CM energies with respect to the QD emission energy. (a)–(d) Energy positions of the two lowest energy TE modes (fundamental CM and the first excited CM_1) of L_3 PC cavities versus PC hole radius measured in 4 different square arrays with $\Delta = 180$, 120, and 90 nm. The gray area denotes the QD ensemble emission energy measured in each square array prior to PC cavity etching.

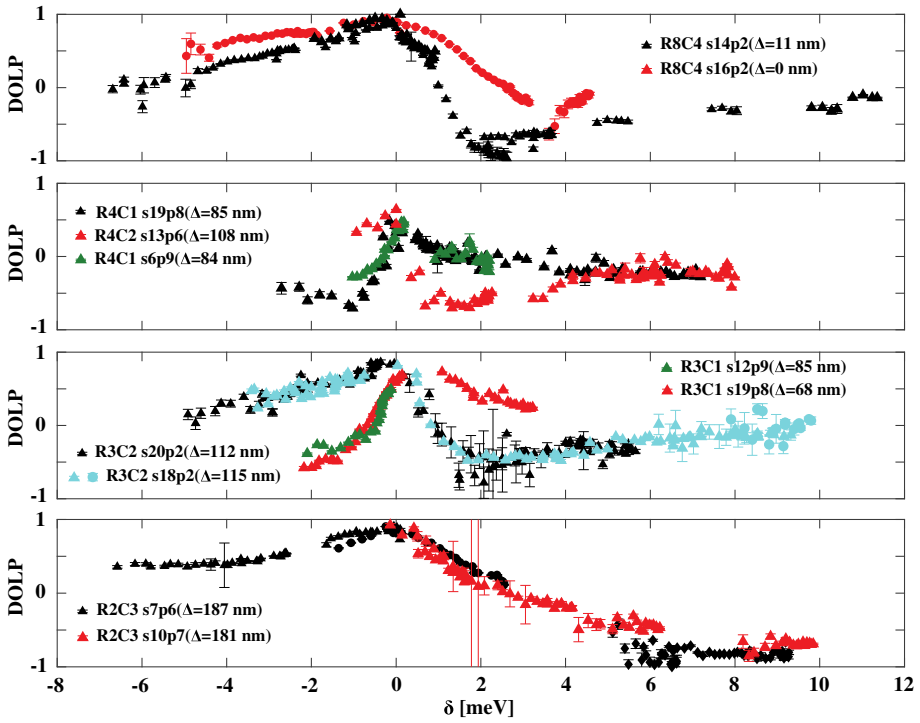

FIG. 12. DOLP traces for different Δ values. CM-QD detuning was modified using a combination of temperature variations and a CM energy tuning using water vapor deposition during the sample cooldown process.

2. Optical mode structure of L_3 PC cavities

Figure 11 shows the measured fundamental CM and the first excited CM_1 resonance energies as a function of PC hole radii measured for several square arrays with nominal $\Delta = 180$, 120, and 90 nm. PC hole radii were designed to provide large positive and negative detunings of the CM

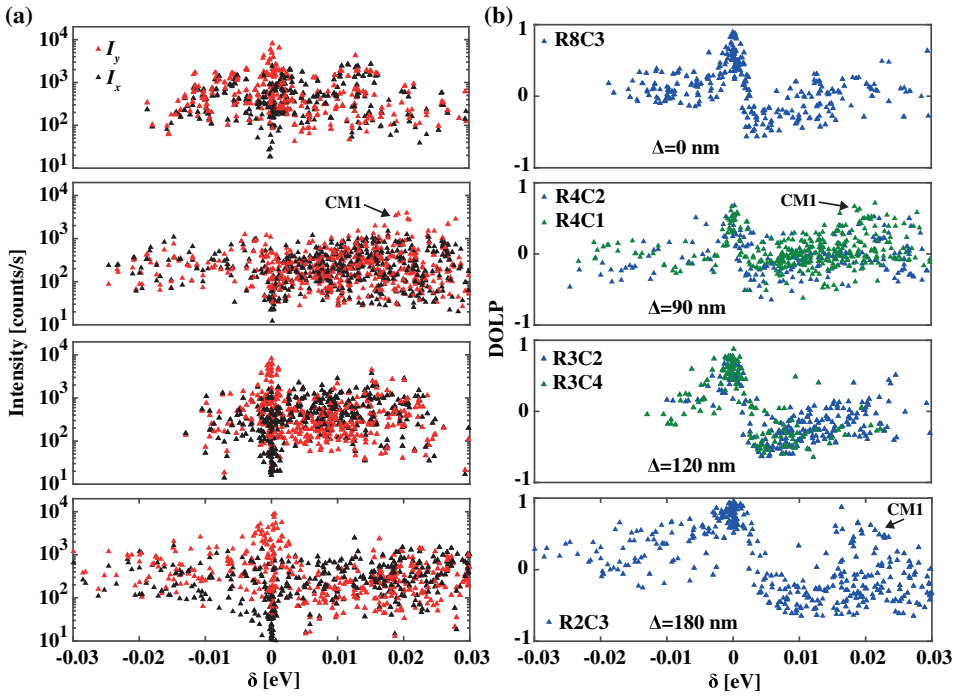

FIG. 13. Statistically yielded polarization-resolved intensities and DOLP spectra. (a) Polarization-resolved intensities of individual lines for $\Delta = 0$, 90, 120, and 180 nm in an L_3 PC cavity. (b) DOLP values extracted from (a). Measurements were performed at 10 K temperature under 300 μW excitation power.

resonance energy with respect to the QD emission energy measured prior to fabrication of PC cavities [55].

3. DOLP traces of single QDs in L_3 PC cavities

Figure 12 shows DOLP traces obtained for different Δ. Corresponding SEM micrographs are shown in Fig. 10. DOLP traces shown in Fig. 12 are well reproduced by the statistically yielded DOLP traces shown in Fig. 13. DOLP statistics were obtained from the polarization-resolved emission spectra measured at the same excitation power $P = 170$ W/cm^2 and temperature $T = 10$ K in PC cavity arrays incorporating single QDs at nominal $\Delta = 0$, 90, 120, and 180 nm. The polarization-resolved spectra of QD emission in PC cavities with different PC radii were measured for up to ∼40 meV of the exciton-CM detuning (see Fig. 13).

APPENDIX B: NUMERICAL AND ANALYTICAL MODELING OF FANO EFFECT IN POLARIZATION-RESOLVED EMISSION OF QDs INTEGRATED WITH PC CAVITIES

1. 3D FEM modeling of the polarized point-dipole emission in a PC cavity

The FEM-based COMSOL MULTIPHYSICS software was used for modeling the emission rates used in Figs. 2(b), 2(d), and 4(d). The calculations were performed in the frequency domain using a point dipole radiation source to represent the quantum dot [57,58]. The refractive index of GaAs was taken to be 3.5, and the slight defect in the GaAs membrane's surface introduced by the fabrication process was modeled as a 30-nm-deep rectangular recess of a 100×100 nm^2 surface area. The size of the holes array of the photonic crystal was limited to 5 periods in every direction around the cavity. This allowed some radiation to escape into the GaAs membrane, yielding the cavity Q factor similar to that obtained in experiments. To make modeling feasible, boundary conditions were used on the xy and xz planes at $z = 0$ and $y = 0$ to achieve symmetry about these planes. Out-coupled power in different polarizations was determined from the electric field intensity distributions ca. 900 nm above the membrane.

Figure 14 shows the x- and y-polarized emission intensities I_x and I_y of the x- and y-oriented dipoles d_x and d_y numerically simulated using 3D FEM. The d_x contribution to the y-polarized emission intensity I_y was insignificant [see Fig. 14(c)] due to a negligible x component of the CM electric field at the probed dipole positions. The strong d_y emission enhancement near 1.4525 eV shows the CM resonance depending on the QD position Δ [Figs. 14(b) and 14(d)]. Destructive

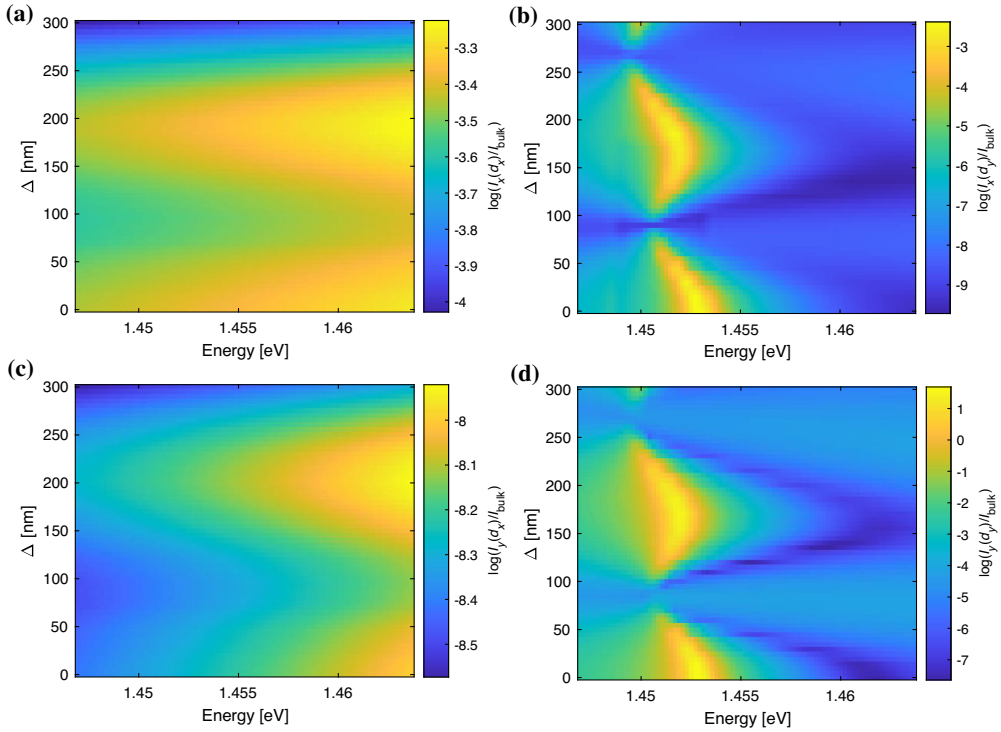

FIG. 14. 3D FEM modeled x- and y-polarized emission intensity components I_x and I_y of the x- and y-oriented dipoles d_x and d_y as a function of the dipole emission energy and position. (a) The x-polarized emission intensity I_x of the x-polarized dipole d_x. (b) The x-polarized emission intensity I_x of the y-polarized dipole d_y. (c) The y-polarized emission intensity I_y of the x-polarized dipole d_x. (d) The y-polarized emission intensity I_y of the y-polarized dipole d_y. Intensities were normalized by the dipole emission intensity in the bulk GaAs.

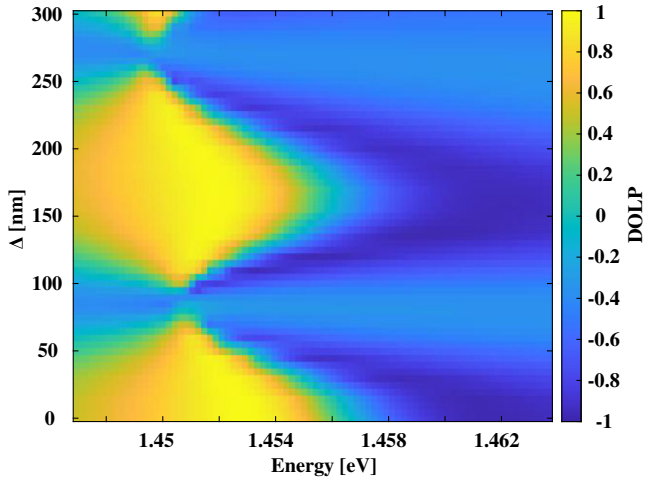

FIG. 15. 3D FEM modeled DOLP as a function of the dipole emission energy and position Δ. DOLP was calculated using the x- and y-polarized intensities I_x and I_y of the x- and y-oriented dipoles d_x and d_y shown in Fig. 14.

interference between the direct and CM-mediated d_y emission channels manifests itself as a strong drop in the x- and y-polarized emission intensities I_x and I_y [see Figs. 14(b) and 14(d)]. We observe $I_x(d_x) \gg I_x(d_y)$ almost everywhere except near the CM resonance [see Figs. 14(a) and 14(b)].

Figure 15 shows the DOLP calculated from the emission intensities shown in Fig. 14, using the expression

$$D = \frac{I_y(d_x) + I_y(d_y) - I_x(d_x) - I_x(d_y)}{I_y(d_x) + I_y(d_y) + I_x(d_x) + I_x(d_y)}. \quad \text{(B1)}$$

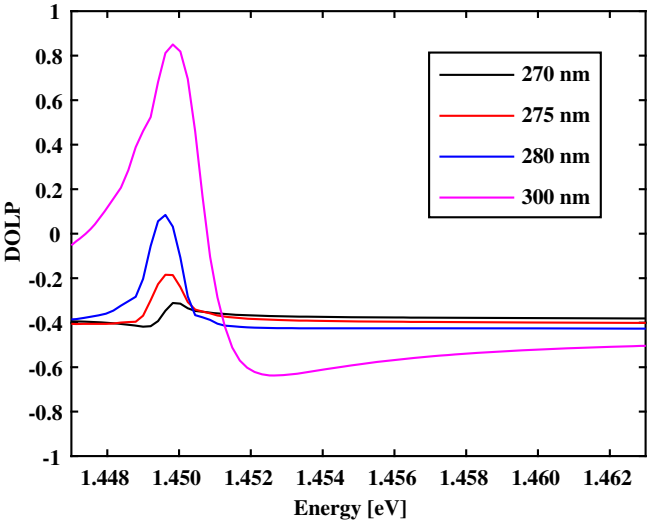

FIG. 16. 3D FEM modeled DOLP traces near the DOLP inversion at Δ ≈ 270 nm. DOLP was calculated as in Fig. 15.

The $I_y(d_y)$ minima visible in Fig. 14(d) correspond to the DOLP minima in Fig. 15.

Figure 16 shows the DOLP modeled near the shift of the DOLP minimum at $\Delta = 275$ nm. At $\Delta = 275$ nm, the curve is flattened, and the minimum is shifted to a lower energy. DOLP at $\Delta = 280$ nm also exhibits a flattened DOLP with a minimum shifted to a higher emission energy.

Figure 17 shows the DOLP spectra modeled with and without the QD recess. The DOLP traces modeled without accounting for the QD recess show the relative phase $\varphi = 0$ for $\Delta = 0$, 45, and 90 nm, which does not agree with the experiment (see Figs. 12 and 13). The agreement is achieved for the DOLP spectra modeled using the 3D FEM approach in the presence of the QD recess [see Fig. 15 and 17(a)].

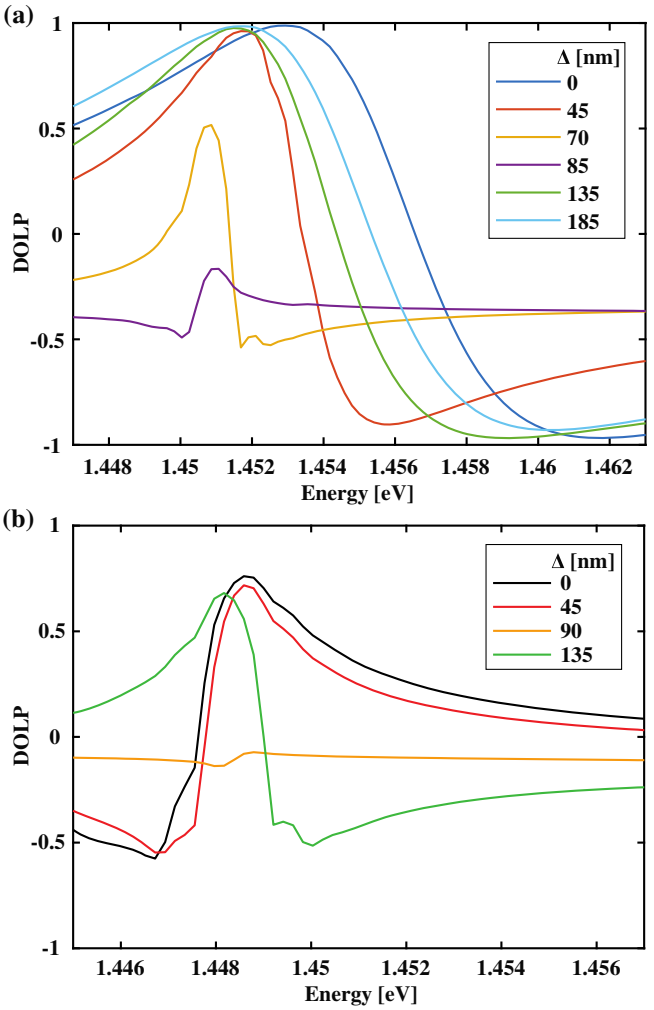

FIG. 17. 3D FEM modeled DOLP for different Δ. (a) DOLP modeled using 3D FEM method considering the QD recess. (b) DOLP modeled using 3D FEM method when ignoring the QD recess. DOLP in (a) and (b) was calculated as in Fig. 15.

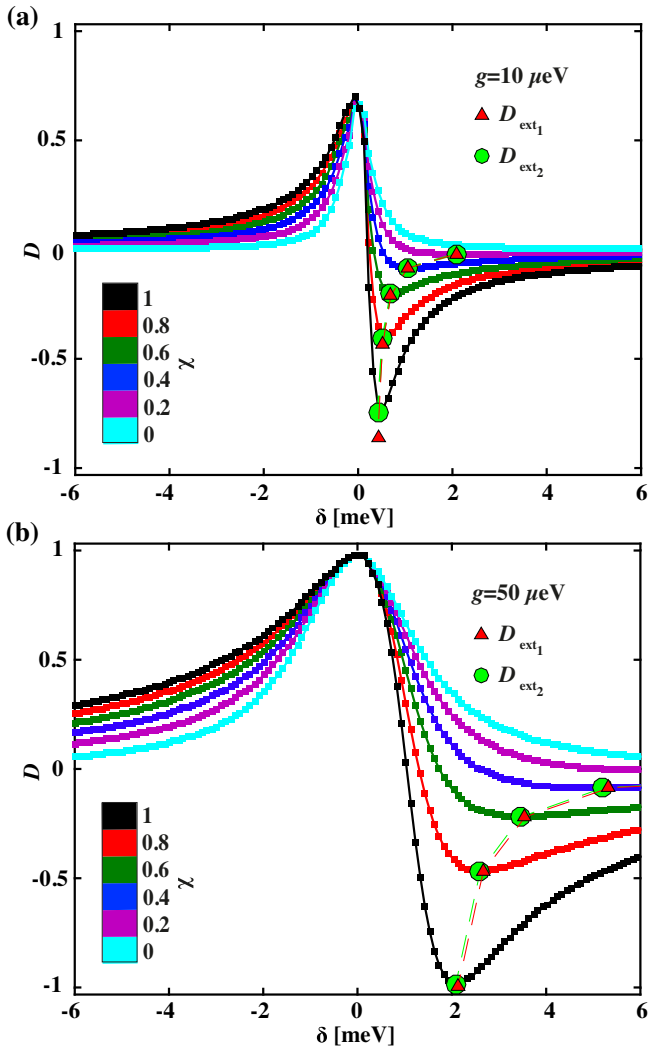

FIG. 18. Numerically and analytically calculated DOLP spectra and the calculated extremum points (δ_{ext},D_{ext}). DOLP modeled using different overlap χ values for $g = 10$ μeV (a) and $g = 50$ μeV (b). In (a) and (b), D_{ext_1} and D_{ext_2} are calculated for factors $\mu_1 = |\delta_{\text{ext}}|/\sqrt{\delta_{\text{ext}}^2 + \gamma_d^2}$ and $\mu_2 = \delta_{\text{ext}}^2/(\delta_{\text{ext}}^2 + \gamma_d^2)$ accounting for spectral diffusion (see Appendix C 2). Modeling parameters are pure dephasing rate $\gamma_d = 120$ μeV, emission rate $\gamma = 0.46$ μeV, CM damping rate $\kappa = 400$ μeV, and relative phase $\varphi = \pi$.

2. Analytical and numerical modeling of DOLP spectra accounting for dephasing processes

Figure 18 shows the comparison of DOLP minima obtained using analytical expressions for δ_{ext} and D_{ext} and DOLP curves numerically modeled using the open Jaynes-Cummings model (see Appendixes C1–C3). Points D_{ext1} and D_{ext2} are calculated using the factors $\mu_1 = |\delta_{\text{ext}}|/\sqrt{\delta_{\text{ext}}^2 + \gamma_d^2}$ and $\mu_2 = \delta_{\text{ext}}^2/(\delta_{\text{ext}}^2 + \gamma_d^2)$ (see Appendix C 2).

Figure 19 shows the comparison between numerically modeled DOLP curves using the open Jaynes-Cummings model and the analytical approximation (see Appendixes C 2 and C 3).

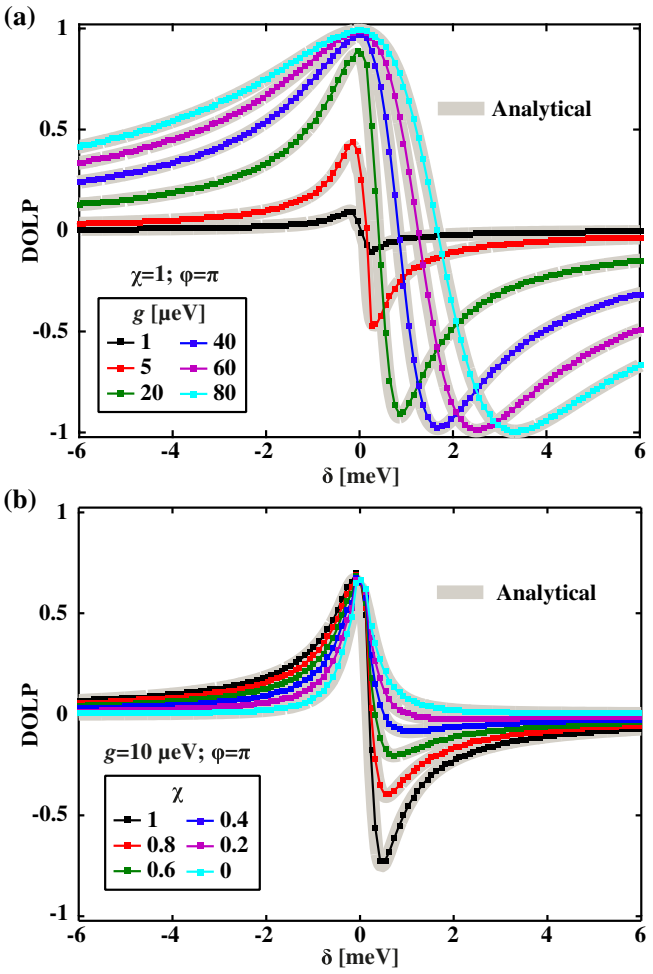

FIG. 19. DOLP spectra for different values of the X-CM coupling strength g (a) and different overlap factors χ (b). The grayed lines were calculated analytically (see Appendix C 5).

APPENDIX C: THEORY

1. Excitonic emission rate W with Yamaguchi approach

Here, we consider independent emission through the y and x polarized modes. In the weak coupling regime and for detuning $\delta \gg g$ in the strong coupling regime, emission through the x polarized modes happens at the excitonic energy with emission rate γ_x. Assuming the same coupling strengths to x and y polarized free-space modes $\eta_{\mathbf{k},x}$ and $\eta_{\mathbf{k},y}$, we obtain $\gamma_x = \gamma_y = \gamma/2$, where the emission rate γ is the total excitonic emission rate through nonbound modes. Following the Yamaguchi approach [30,42], we consider the Hamiltonian $\hat{\mathcal{H}} = \hat{\mathcal{H}}_0 + \hat{\mathcal{H}}_{\text{int}} + \hat{\mathcal{H}}_R$ that drives the interaction in the exciton-CM system coupled to the common reservoir of the y-polarized radiation modes. The terms $\hat{\mathcal{H}}_0$, $\hat{\mathcal{H}}_{\text{int}}$, and $\hat{\mathcal{H}}_R$ are defined as

$$\hat{\mathcal{H}}_0 = \hbar\omega_{\mathrm{QD}}\hat{\sigma}^\dagger\hat{\sigma} + \hbar\omega_{\mathrm{CM}}\hat{a}^\dagger_{\mathrm{CM}}\hat{a}_{\mathrm{CM}} + \hbar\sum_{\mathbf{k}}\omega_{\mathbf{k}}\hat{b}^\dagger_{\mathbf{k}}\hat{b}_{\mathbf{k}}, \quad \text{(C1)}$$

$$\hat{\mathcal{H}}_{\mathrm{int}} = \hbar(g\hat{\sigma}^\dagger\hat{a}_{\mathrm{CM}} + \mathrm{H.c.}), \quad \text{(C2)}$$

$$\hat{\mathcal{H}}_R = \hbar\sum_{\mathbf{k}}(\xi_{\mathbf{k},y}\hat{a}^\dagger_{\mathrm{CM}}\hat{b}_{\mathbf{k}} + \mathrm{H.c.}) + \hbar\sum_{\mathbf{k}}(\eta_{\mathbf{k},y}\hat{\sigma}^\dagger\hat{b}_{\mathbf{k}} + \mathrm{H.c.}), \quad \text{(C3)}$$

where $\hat{\sigma}$, $\hat{a}_{\mathrm{CM}}$, and $\hat{b}_{\mathbf{k}}$ are the annihilation operators of the QD exciton, CM, and free-space radiation modes. The coupling strengths g, $\xi_{\mathbf{k},y}$, and $\eta_{\mathbf{k},y}$ can be written as $g = |g|e^{i\varphi_g}$, $\eta_{\mathbf{k},y} = |\eta_{\mathbf{k},y}|e^{i\varphi_{\mathbf{k},\eta}}$. and $\xi_{\mathbf{k},y} = |\xi_{\mathbf{k},y}|e^{i\varphi_{\mathbf{k},\xi}}$.

Considering the low pumping regime, we restrict the photon wave function basis to a set of Fock states corresponding to 0 or 1 photons in the CM and free-space radiation modes. The two-level QD excitonic transition is between ground and excited states $|g\rangle$ and $|e\rangle$. Then, the superposition wave function is written as

$$|\psi(t)\rangle = a(t)e^{-i\omega_{QD}t}|e, 0_{\mathrm{CM}}, 0_{\mathbf{k}}\rangle + c(t)e^{-i\omega_{\mathrm{CM}}t}|g, 1_{\mathrm{CM}}, 0_{\mathbf{k}}\rangle + \sum_{\mathbf{k}} b_{\mathbf{k}}(t)e^{-i\omega_{\mathbf{k}}t}|g, 0_{\mathrm{CM}}, 1_{\mathbf{k}}\rangle, \quad \text{(C4)}$$

where $|e, 0_{\mathrm{CM}}, 0_{\mathbf{k}}\rangle$, $|g, 1_{\mathrm{CM}}, 0_{\mathbf{k}}\rangle$, and $|g, 0_{\mathrm{CM}}, 1_{\mathbf{k}}\rangle$ are the Fock wave functions corresponding to a single excitation in the system, a single photon in the CM, and a single photon in the free-space mode with wave vector $\mathbf{k}$. Looking for the evolution of the amplitude probabilities $a(t)$, $c(t)$, and $b_{\mathbf{k}}(t)$, we solve Schrödinger's equation in the framework of the Weisskopf-Wigner approximation and obtain the following equations of motion:

$$\frac{da(t)}{dt} = -\left(ige^{i\varphi_g} + \tilde{\chi}\frac{\sqrt{\gamma_y\kappa}}{2}\right)c(t)e^{i\delta t} - \frac{\gamma_y}{2}a(t),$$
$$\frac{dc(t)}{dt} = -\left(ige^{-i\varphi_g} + \tilde{\chi}^*\frac{\sqrt{\gamma_y\kappa}}{2}\right)a(t)e^{-i\delta t} - \frac{\kappa}{2}c(t), \quad \text{(C5)}$$

where γ and κ are dissipation rates of the exciton and CM through radiation modes, while the complex overlap term can be written as $\tilde{\chi} = \sum_{\mathbf{k}}\eta_{\mathbf{k},y}\xi^*_{\mathbf{k},y}/\sqrt{\sum_{\mathbf{k}}\eta_{\mathbf{k},y}\eta^*_{\mathbf{k},y} \times \sum_{\mathbf{k}}\xi_{\mathbf{k},y}\xi^*_{\mathbf{k},y}}$. The complex overlap could be rewritten as $\tilde{\chi} = \chi e^{-i\varphi_{\xi\eta}}$, where $0 \le \chi \le 1$ and $\varphi_{\xi\eta} \in [0, \pi]$. The complex phase $\varphi_{\xi\eta}$ has the meaning of the phase difference between the CM and exciton coupling channels to the common radiation reservoir. In the following, we assume that $\varphi_{\mathbf{k},\eta}$ and $\varphi_{\mathbf{k},\xi}$ are independent on the wave vector $\mathbf{k}$; that is, $\varphi_{\mathbf{k},\eta} = \varphi_\eta$ and $\varphi_{\mathbf{k},\xi} = \varphi_\xi$. Thus, we obtain $\varphi_{\xi\eta} = \varphi_\xi - \varphi_\eta$. Solving the eigenvalue problem of this set of differential equations, one can retrieve the emission rate of the exciton. The eigenenergies read

$$\gamma_\pm = -\frac{1}{2}\left(\frac{\kappa+\gamma_y}{2} - i\delta\right) \pm \frac{1}{2}\sqrt{\left(\frac{\kappa-\gamma_y}{2} - i\delta\right)^2 - 4\left(|g|^2 - i\chi|g|\sqrt{\gamma_y\kappa}\cos\varphi - \frac{\chi^2\gamma_y\kappa}{4}\right)}, \quad \text{(C6)}$$

where we introduced the relative phase $\varphi = \varphi_g + \varphi_\xi - \varphi_\eta$ that has the meaning of the phase difference between excitonic emission through bound and nonbound modes. The exciton decay rate can be found as

$$W = \begin{cases} -2\mathrm{Re}(\gamma_+) & \kappa > \gamma \\ -2\mathrm{Re}(\gamma_-) & \kappa < \gamma. \end{cases} \quad \text{(C7)}$$

For typical QD-PC cavity systems, we have $\kappa \gg \gamma$, and the excitonic emission rate through y polarized modes reads

$$W_y(\delta) = \frac{\kappa+\gamma_y}{2} - \mathrm{Re}\left[\left(\frac{\kappa-\gamma_y}{2} - i\delta\right)^2 - (2|g| - i\chi\sqrt{\gamma_y\kappa}e^{-i\varphi}) \times (2|g| - i\chi\sqrt{\gamma_y\kappa}e^{i\varphi})\right]^{1/2}. \quad \text{(C8)}$$

The degree of linear polarization is given by $D = (I_y - I_x)/(I_y + I_x)$, where I_x and I_y are the x and y polarized emission intensities. For excitonic transitions with fractional or zero excited state pseudospins, the dipole projections on two perpendicular axes, e.g., x and y axis, have the same absolute amplitudes. Therefore, $D = (W_y - \alpha\gamma_x)/(W_y + \alpha\gamma_x)$, where α is the ratio between the x- and y-polarized emission collection efficiencies of the optical system. For $\alpha = 1$, we obtain

$$D = \frac{\kappa - 2\mathrm{Re}\left[\sqrt{(\frac{\kappa-\gamma_y}{2} - i\delta)^2 - 4(|g|^2 - i\chi|g|\sqrt{\gamma_y\kappa}\cos\varphi - \frac{\chi^2\gamma_y\kappa}{4})}\right]}{\kappa + 2\gamma_y - 2\mathrm{Re}\left[\sqrt{(\frac{\kappa-\gamma_y}{2} - i\delta)^2 - 4(|g|^2 - i\chi|g|\sqrt{\gamma_y\kappa}\cos\varphi - \frac{\chi^2\gamma_y\kappa}{4})}\right]}. \quad \text{(C9)}$$

The emission rate W_y was simulated with $\gamma_y = 0.4$ μeV, $\kappa = 600$ μeV, and $\chi = 0.95$.

2. Detuning and the degree of linear polarization at the interference maximum

In order to investigate our system at the interference maximum, we describe the X-CM system in a polariton basis and write $|g,0\rangle = |g\rangle|0_{\mathrm{CM}}\rangle$, $|-,1\rangle = \cos\beta|e\rangle|0_{\mathrm{CM}}\rangle - \sin\beta|g\rangle|1_{\mathrm{CM}}\rangle$, and $|+,1\rangle = \sin\beta|e\rangle|0_{\mathrm{CM}}\rangle + \cos\beta|g\rangle|1_{\mathrm{CM}}\rangle$, where $|g\rangle$ and $|e\rangle$ are the ground and excited excitonic states, $|0_{\mathrm{CM}}\rangle$ and $|1_{\mathrm{CM}}\rangle$ are the empty and occupied single-photon CM states, the parameter β is given by $\beta = \tan^{-1}[2g/(\sqrt{4g^2+\delta^2}-\delta)]$, and $\delta = \omega_{QD} - \omega_{\mathrm{CM}}$ is the X-CM detuning. The expected interference in two-level system decay through y polarized modes appears from the analysis of the equation of motion of the total system wave function:

$$|\psi(\mathrm{t})\rangle = A(t)e^{-i\omega_- t}|-,1\rangle|0_{\mathbf{k},\rho}\rangle + B(t)e^{-i\omega_+ t}|+,1\rangle|0_{\mathbf{k},\rho}\rangle + \sum_{\mathbf{k},\rho} b_{\mathbf{k},\rho}(t)e^{-i\omega_{\mathbf{k}} t}|g,0\rangle|1_{\mathbf{k},\rho}\rangle, \tag{C10}$$

where $|0_{\mathbf{k},\rho}\rangle$ and $|1_{\mathbf{k},\rho}\rangle$ are the free-space photon wave functions (FMs), and $\mathbf{k}$ and $\rho = \{x,y\}$ are the FM wave vector and polarization, respectively.

The system Hamiltonian is $\hat{\mathcal{H}}_P = \hat{\mathcal{H}}_0 + \hat{\mathcal{H}}_R$, with

$$\hat{\mathcal{H}}_0 = \hbar\omega_- \hat{c}_-^\dagger \hat{c}_- + \hbar\omega_+ \hat{c}_+^\dagger \hat{c}_+, \tag{C11}$$

$$\hat{\mathcal{H}}_R = \hbar\sum_{\mathbf{k},\rho}(p_{\mathbf{k},\rho}\hat{c}_-^\dagger b_{\mathbf{k},\rho} + \mathrm{H.c.}) + \hbar\sum_{\mathbf{k},\rho}(f_{\mathbf{k},\rho}\hat{c}_+^\dagger b_{\mathbf{k},\rho} + \mathrm{H.c.}), \tag{C12}$$

where $\hat{c}_-$ and $\hat{c}_+$ are the annihilation operators of polariton states $|-,1\rangle$ and $|+,1\rangle$ and $p_{\mathbf{k},\rho}$ and $f_{\mathbf{k},\rho}$ are the polariton coupling strengths with the radiation modes. These coupling strengths can be rewritten in terms of coupling strengths $\eta_{\mathbf{k},\rho}$ and $\xi_{\mathbf{k},\rho}$ [see Ref. [30] and Fig. 1(a)] as $p_{\mathbf{k},\rho} = \eta_{\mathbf{k},\rho}\cos\beta - \xi_{\mathbf{k},\rho}\sin\beta$ and $f_{\mathbf{k},\rho} = \eta_{\mathbf{k},\rho}\sin\beta + \xi_{\mathbf{k},\rho}\cos\beta$. Since the CM in our system is strongly y polarized, we consider the CM coupling only to the x-polarized FMs; i.e., $\xi_{\mathbf{k},x} = 0$. The coupling coefficients are $g = |g|e^{i\varphi_g}$, $\eta_{\mathbf{k},y} = |\eta_{\mathbf{k},y}|e^{i\varphi_\eta}$, and $\xi_{\mathbf{k},y} = |\xi_{\mathbf{k},y}|e^{i\varphi_\xi}$. The relative phase between the direct and CM-mediated decay paths of the TLS is $\varphi = \varphi_g + \varphi_\xi - \varphi_\eta$.

The polariton probability amplitudes $A(t)$ and $B(t)$ in the Weisskopf-Wigner approximation are driven by the following differential equations:

$$\frac{dA(t)}{dt} = -\frac{\Gamma_A}{2}A(t) - \frac{\Gamma_{AB}}{2}B(t)e^{i(\omega_- - \omega_+)t},$$
$$\frac{dB(t)}{dt} = -\frac{\Gamma_B}{2}B(t) - \frac{\Gamma_{AB}^*}{2}A(t)e^{i(\omega_+ - \omega_-)t}, \tag{C13}$$

where $\Gamma_A = \gamma_x\cos^2\beta + \Gamma_-$, $\Gamma_B = \gamma_x\sin^2\beta + \Gamma_+$, and $\Gamma_{AB} = (\gamma_x\sin 2\beta)/2 + \vartheta\sqrt{\Gamma_-\Gamma_+}$ with $\Gamma_\pm = (\kappa+\gamma_y)/2 \pm \{[(\kappa-\gamma_y)\cos 2\beta]/2 + \chi\sqrt{\gamma_y\kappa}\cos\varphi\sin 2\beta\}$. The QD emission rate is $\gamma_\rho = [(2\pi)/\hbar]\sum_{\mathbf{k}}\eta_{\mathbf{k},\rho}\eta_{\mathbf{k},\rho}^*$, where $\rho = \{x,y\}$, the CM damping rate is $\kappa = [(2\pi)/\hbar]\sum_{\mathbf{k}}\xi_{\mathbf{k},V}\xi_{\mathbf{k},V}^*$, and the overlap between QD and CM emission patterns is $\chi = |\sum_{\mathbf{k}}\eta_{\mathbf{k},y}\xi_{\mathbf{k},y}^*|/\sqrt{\sum_{\mathbf{k}}\eta_{\mathbf{k},y}\eta_{\mathbf{k},y}^* \times \sum_{\mathbf{k}}\xi_{\mathbf{k},y}\xi_{\mathbf{k},y}^*}$. Factor $\vartheta = \sum_{\mathbf{k}}p_{\mathbf{k},y}f_{\mathbf{k},y}^*/\sqrt{\sum_{\mathbf{k}}p_{\mathbf{k},y}p_{\mathbf{k},y}^* \times \sum_{\mathbf{k}}f_{\mathbf{k},y}f_{\mathbf{k},y}^*}$ is a complex number ($|\vartheta| \le 1$) reflecting the overlap and the phase shift of radiation modes to which the polariton decays. For typical X-CM damping parameters, we have $\gamma_y \ll \kappa$ and the emission rates Γ_+ and Γ_- have their minimum values at extremum exciton-CM detuning:

$$\delta_{\mathrm{ext}} = \frac{g}{\chi\cos\varphi}\left(\sqrt{\frac{\gamma_y}{\kappa}} - \sqrt{\frac{\kappa}{\gamma_y}}\right) \tag{C14}$$

if $\delta_{\mathrm{ext}}(\kappa-\gamma_y) > 0$ and $\delta_{\mathrm{ext}}(\kappa-\gamma_y) < 0$, respectively. The relative phase $\varphi = \varphi_g + \varphi_\xi - \varphi_\eta$ defines the detuning sign at which the Fano interference appears. For a typical X-CM system, we have $\kappa \gg \gamma_y$ providing the detuning $|\delta_{\mathrm{ext}}| \gg g$. Therefore, the term $(\gamma_x/2)\sin 2\beta$ can be neglected at δ_{ext} and the polariton decay rates through y-polarized modes are determined solely by Γ_+ and Γ_-. The emission at the exciton energy originates mainly from the exitonlike polariton state $|-,1\rangle$ ($|+,1\rangle$), if $\delta < 0$ ($\delta > 0$). Since for a typical QD-PC cavity system we have $\gamma_y \ll \kappa$, the detuning δ_{ext} corresponds to the minimum of the excitonic emission rate W_y through the y polarized modes.

For charged exciton and biexciton transitions or any other excitonic transition with zero or fractional pseudospin and equal dipole matrix elements along x and y axes, the degree of linear polarization $D = (I_y - I_x)/(I_y + I_x)$ can be rewritten as $D = (W_y - \alpha * \gamma_x)/(W_y + \alpha * \gamma_x)$, where W_y and γ_x are the emission rates through y and x polarized modes and $\alpha \approx 1$ is the ratio between the y- and x-polarized emission powers collected by the objective [see Fig. 1(a)]. The coupling efficiency $\alpha \approx 1$ provides $D = (W_y - \gamma_x)/(W_y + \gamma_x)$. Since transitions detuned by several tens of meV from the PC cavity modes are essentially unpolarized, we have $D \approx 0$.

For detuning $|\delta| \gg |g|$, the emission through the x-polarized modes appears mainly at the energy of the excitonic transition. For $|\delta| \gg |g|$, the emission rate W_y can be approximated as $\Gamma_\pm$, providing

$$W_y \approx \frac{\kappa+\gamma_y}{2} \pm \left[\frac{\kappa-\gamma_y}{2}\cos 2\beta + \mu\chi\sqrt{\gamma_y\kappa}\cos\varphi\sin 2\beta\right], \tag{C15}$$

where the factor μ takes into account the decoherence due to pure dephasing processes with the dephasing rate γ_d.

The emission rate at δ_{ext} is $W_y(\delta_{\text{ext}}) = (1-\mu^2\chi^2\cos^2\varphi)\gamma_y$, leading to

$$D = \frac{-\mu^2\chi^2\cos^2\varphi}{2-\mu^2\chi^2\cos^2\varphi}. \tag{C16}$$

Scaling factors $\mu_1 = |\delta_{\text{ext}}|/\sqrt{\delta_{\text{ext}}^2+\gamma_d^2}$ and $\mu_2 = \delta_{\text{ext}}^2/(\delta_{\text{ext}}^2+\gamma_d^2)$ provide

$$D_{\text{ext},1} = -\frac{(\chi\cos\varphi)^2\delta_{\text{ext}}^2}{[2-(\chi\cos\varphi)^2]\delta_{\text{ext}}^2+2\gamma_d^2}, \tag{C17}$$

$$D_{\text{ext},2} = -\frac{(\chi\cos\varphi)^2\delta_{\text{ext}}^4}{2(\delta_{\text{ext}}^2+\gamma_d^2)^2-(\chi\cos\varphi)^2\delta_{\text{ext}}^4}, \tag{C18}$$

assuming that $\gamma_x = \gamma_y$. The best approximation for the modeled DOLP traces is obtained for $D_{\text{ext},2}$.

3. Numerical modeling of the DOLP curves using open Jaynes-Cummings model

The radiating quantum dot is modeled as a two-level system with Bohr frequency $\omega_0/(2\pi)$ coupled to a cavity mode at frequency $\omega_{\text{CM}}/(2\pi)$. The detuning between the TLS and cavity mode energies is $\hbar\delta = \hbar\omega_0 - \hbar\omega_{\text{CM}}$. The Hamiltonian describing the system in the rotating wave approximation is

$$H = \hbar\omega_{\text{CM}}a^\dagger a + \hbar\omega_0\sigma^+\sigma^- + \hbar g(\sigma^+a + a^\dagger\sigma^-), \tag{C19}$$

where σ^- (σ^+) is the lowering (raising) operator of TLS and a ($a^\dagger$) is the lowering (raising) operator of CM. Losses and solid-state specific phenomena are added using the master equation formalism. The evolution of the density matrix ρ of the system formed by the QD and the cavity is given by

$$\dot{\rho} = -\frac{i}{\hbar}[H,\rho] - \frac{1}{2}\left\{\sum_l L_l^\dagger L_l, \rho\right\} + \sum_l L_l\rho L_l^\dagger, \tag{C20}$$

which is compatible with the framework used to perform the numerical simulations [59]. We introduce the following quantum collapse operators:

(i) $L_\gamma = \sqrt{\gamma}\sigma^-$ describes the QD spontaneous emission at rate γ;
(ii) $L_\kappa = \sqrt{\kappa}a$ accounts for the cavity losses at rate κ;
(iii) $L_P = \sqrt{P}\sigma^+$ describes incoherent pumping of the QD at rate P;
(iv) $L_{\gamma_d} = \sqrt{\gamma_d}/2\sigma^z$ models effective pure dephasing of the QD, causing a Lorentzian broadening with FWHM γ_d;
(v) $L_{\text{ph}} = \sqrt{\Gamma^{\text{ph}}}\sigma^-a^\dagger$ describes phonon scattering, effectively transferring excitations from the QD to the cavity.

The rate Γ^{ph} is a function of TLS-CM detuning and temperature. It was calculated using the following microscopic description of the exciton-phonon interaction [60,61]. The transfer of excitations from the QD to the off-resonant CM via the absorption or emission of a phonon is described by the quantum collapse operator $L_{\text{ph}} = \sqrt{\Gamma^{\text{ph}}}\sigma^-a^\dagger$ that accounts for the decay from the state $|e\rangle \otimes |n=0\rangle$ to the state $|g\rangle \otimes |n=1\rangle$ at rate Γ^{ph}, with $|e\rangle$ ($|g\rangle$) being the excited (ground) state of the exciton and $\{|g\rangle\}_{n\in N}$ being the Fock space of the quantized CM. Here we neglect the backscattering term $\sqrt{\Gamma^{\text{ph}}(-\delta)}\sigma^+a$ describing the phonon-mediated feeding of the QD by the CM, which is reasonable in the bad cavity regime ($\kappa \gg \gamma$). The phonon scattering rate Γ^{ph} accounting for the phonon-assisted decay of the QD exciton into the CM is given in Ref. [47].

The master equation (C20) is solved numerically using the quantum optics toolbox QuTip to obtain the steady-state power spectra of the TLS and CM. Exciton, CM, and X-CM interference steady-state power spectra $S_X(\omega)$, $S_{\text{CM}}(\omega)$, and $S_{\text{int}}(\omega)$ are given by

$$S_X(\omega) = \int_{-\infty}^{\infty}\lim_{t\to\infty}\sigma^+(t+\tau)\sigma^-(t)e^{-i\omega\tau}d\tau, \tag{C21}$$

$$S_{\text{CM}}(\omega) = \int_{-\infty}^{\infty}\lim_{t\to\infty}a^\dagger(t+\tau)a(t)e^{-i\omega\tau}d\tau, \tag{C22}$$

$$S_{\text{int}}(\omega) = \int_{-\infty}^{\infty}\lim_{t\to\infty}a^\dagger(t+\tau)\sigma^-(t)e^{-i\omega\tau}d\tau. \tag{C23}$$

In the above integrals, the correlation functions $\langle A(t+\tau)B(t)\rangle$ are calculated numerically using the exponential-series-based solver essolve [59] that computes the nonunitary time evolution of the system operators A and B by solving the master equation. The Fourier transform of the steady-state correlation function is then performed semianalytically [59], giving the power spectrum which is then used to compute the degree of linear polarization of the excitonic spectrum. We obtain the x- and y-polarized excitonic emission intensities by fitting the x- and y-polarized emission spectra $I_x(\omega)$ and $I_y(\omega)$ calculated as

$$I_x(\omega) = \frac{\gamma}{2}|S_X(\omega)|^2, \tag{C24}$$

$$I_y(\omega) = \frac{\gamma}{2}|S_X(\omega)|^2 + \kappa|S_{\text{CM}}(\omega)|^2 + \sqrt{\frac{\gamma\kappa}{2}}[S_{\text{int}}(\omega) + S_{\text{int}}^*(\omega)]\chi\cos\varphi. \tag{C25}$$

Here, $\chi\cos\varphi$ accounts for the interference between excitonic emission into free-space modes and the emission mediated by the CM. The degree of linear polarization is obtained as $D(\omega) = \{[I_y(\omega)-I_x(\omega)]/[I_y(\omega)+I_x(\omega)]\}$.

4. Correction of DOLP curves in the case of the polarizer misalignment

In the case of misalignment between the transmission polarization axis of the polarization analyzer and the CM linear polarization, excitonic DOLP values can be corrected using the measured CM polarization plane. Excitonic DOLP values D_{ideal} for the case of an ideal alignment between the CM and the polarization analyzer y axis are given by $D_{\text{ideal}} = D_{\text{meas}}/D_{\text{CM}}$, where D_{meas} and D_{CM} are the measured excitonic DOLP values and the CM DOLP. Note that $D_{\text{ideal}} = [I_y(\omega) - I_x(\omega)]/[I_y(\omega) + I_x(\omega)]$, $D_{\text{CM}} = \cos^2\vartheta - \sin^2\vartheta$, and $D_{\text{meas}} = [I_y(\omega) - I_x(\omega)] \times (\cos^2\vartheta - \sin^2\vartheta)/[I_y(\omega) + I_x(\omega)] = D_{\text{ideal}} D_{\text{CM}}$. Here, ϑ is the misalignment angle between the transmission axis of the polarization analyzer and the CM linear polarization plane. We also assumed that the CM is perfectly linearly polarized, which agrees with the experimental results. Using this method, we corrected DOLP curves for $\Delta =$ 42 and 180 nm (see Appendix A 3).

5. Analytical modeling of DOLP curves

The x- and y-polarized intensities of the X-CM emission can be approximated as

$$I_x = \frac{\gamma}{2} p, \tag{C26}$$

$$I_y(\delta) = \left(\alpha \gamma_{\text{CM}}(\delta) + \frac{\delta^2 \sqrt{2\alpha\gamma_{\text{CM}}(\delta)}\gamma\chi\cos\varphi}{\delta^2 + \gamma_d^2} + \frac{\gamma}{2} \right) p, \tag{C27}$$

where $\gamma_{\text{CM}}(\delta) = (\gamma/2) F_P (1 + \gamma_d/\kappa)/[4\delta^2/\kappa^2 + (1 + \gamma_d/\kappa)^2]$ and γ are, respectively, the exciton emission rate through the CM and the nonbound modes, α is the scaling parameter that takes into account emission at the exciton energy, and p is the exciton average occupation. We set $p = 1$ in the modeling. Parameters χ, φ, γ_d, κ, and δ are as described above. The factor $\delta^2/(\delta^2 + \gamma_d^2)$ in $I_y(\delta)$ describes damping of the coherence between the two decay channels by decreasing the weight of the interference term while approaching the zero detuning.

The degree of linear polarization $D(\delta) = [I_y(\delta) - I_x]/[I_y(\delta) + I_x]$ is in good agreement with the data modeled using the open Janes-Cummings model (see Figs. 18 and 13) with the following expression for the scaling parameter:

$$\alpha = \frac{\kappa + \gamma_d + \gamma + \kappa \frac{\delta^2}{\gamma_d^2}}{\kappa + \gamma_d + \gamma + (\kappa + \gamma_d + \gamma) \frac{\delta^2}{\gamma_D^2}}. \tag{C28}$$

[1] E. M. Purcell, H. C. Torrey, and R. V. Pound, *Resonance Absorption by Nuclear Magnetic Moments in a Solid*, Phys. Rev. **69**, 37 (1946).

[2] P. Michler, A. Kiraz, C. Becher, W. V Schoenfeld, P. M. Petroff, L. Zhang, E. Hu, and A. Imamoglu, *A Quantum Dot Single-Photon Turnstile Device*, Science **290**, 2282 (2000).

[3] E. Moreau, I. Robert, J. M. Gérard, I. Abram, L. Manin, and V. Thierry-Mieg, *Single-Mode Solid-State Single Photon Source Based on Isolated Quantum Dots in Pillar Microcavities*, Appl. Phys. Lett. **79**, 2865 (2001).

[4] C. Santori, D. Fattal, J. Vučković, G. S. Solomon, and Y. Yamamoto, *Indistinguishable Photons from a Single-Photon Device*, Nature (London) **419**, 594 (2002).

[5] N. Somaschi, V. Giesz, L. De Santis, J. C. Loredo, M. P. Almeida, G. Hornecker, S. L. Portalupi, T. Grange, C. Antón, J. Demory, C. Gómez, I. Sagnes, N. D. Lanzillotti-Kimura, A. Lemaítre, A. Auffeves, A. G. White, L. Lanco, and P. Senellart, *Near-Optimal Single-Photon Sources in the Solid State*, Nat. Photonics **10**, 340 (2016).

[6] X. Ding, Y. He, Z. C. Duan, N. Gregersen, M. C. Chen, S. Unsleber, S. Maier, C. Schneider, M. Kamp, S. Höfling, C. Y. Lu, and J. W. Pan, *On-Demand Single Photons with High Extraction Efficiency and Near-Unity Indistinguishability from a Resonantly Driven Quantum Dot in a Micropillar*, Phys. Rev. Lett. **116**, 020401 (2016).

[7] L. Sapienza, M. Davanço, A. Badolato, and K. Srinivasan, *Nanoscale Optical Positioning of Single Quantum Dots for Bright and Pure Single-Photon Emission*, Nat. Commun. **6**, 7833 (2015).

[8] M. Arcari, I. Söllner, A. Javadi, S. Lindskov Hansen, S. Mahmoodian, J. Liu, H. Thyrrestrup, E. H. Lee, J. D. Song, S. Stobbe, and P. Lodahl, *Near-Unity Coupling Efficiency of a Quantum Emitter to a Photonic Crystal Waveguide*, Phys. Rev. Lett. **113**, 093603 (2014).

[9] B. Rigal, B. Dwir, A. Rudra, I. Kulkova, A. Lyasota, and E. Kapon, *Single Photon Extraction and Propagation in Photonic Crystal Waveguides Incorporating Site-Controlled Quantum Dots*, Appl. Phys. Lett. **112**, 051105 (2018).

[10] X. Zhou, R. Uppu, Z. Liu, C. Papon, R. Schott, A. D. Wieck, A. Ludwig, P. Lodahl, and L. Midolo, *On-Chip Nanomechanical Filtering of Quantum-Dot Single-Photon Sources*, Laser Photonics Rev. **14**, 1900404 (2020).

[11] S. Slussarenko and G. J. Pryde, *Photonic Quantum Information Processing: A Concise Review*, Appl. Phys. Rev. **6**, 041303 (2019).

[12] A. Auffèves, D. Gerace, J. M. Gérard, M. F. Santos, L. C. Andreani, and J. P. Poizat, *Controlling the Dynamics of a Coupled Atom-Cavity System by Pure Dephasing*, Phys. Rev. B **81**, 245419 (2010).

[13] D. Englund, D. Fattal, E. Waks, G. Solomon, B. Zhang, T. Nakaoka, Y. Arakawa, Y. Yamamoto, and J. Vuckovic, *Controlling the Spontaneous Emission Rate of Single Quantum Dots in a Two-Dimensional Photonic Crystal*, Phys. Rev. Lett. **95**, 013904 (2005).

[14] D. G. Gevaux, A. J. Bennett, R. M. Stevenson, A. J. Shields, P. Atkinson, J. Griffiths, D. Anderson, G. A. C. Jones, and D. A. Ritchie, *Enhancement and Suppression of Spontaneous Emission by Temperature Tuning InAs Quantum Dots to Photonic Crystal Cavities*, Appl. Phys. Lett. **88**, 131101 (2006).

[15] T. Jakubczyk, H. Franke, T. Smoleński, M. Ściesiek, W. Pacuski, A. Golnik, R. Schmidt-Grund, M. Grundmann,

C. Kruse, D. Hommel, and P. Kossacki, *Inhibition and Enhancement of the Spontaneous Emission of Quantum Dots in Micropillar Cavities with Radial-Distributed Bragg Reflectors*, ACS Nano **8**, 9970 (2014).

[16] M. Bayer, T. L. Reinecke, F. Weidner, A. Larionov, A. McDonald, and A. Forchel, *Inhibition and Enhancement of the Spontaneous Emission of Quantum Dots in Structured Microresonators*, Phys. Rev. Lett. **86**, 3168 (2001).

[17] J. Johansen, B. Julsgaard, S. Stobbe, J. M. Hvam, and P. Lodahl, *Probing Long-Lived Dark Excitons in Self-Assembled Quantum Dots*, Phys. Rev. B **81**, 081304(R) (2010).

[18] Q. Wang, S. Stobbe, and P. Lodahl, *Mapping the Local Density of Optical States of a Photonic Crystal with Single Quantum Dots*, Phys. Rev. Lett. **107**, 167404 (2011).

[19] K. H. Madsen, P. Kaer, a. Kreiner-Møller, S. Stobbe, A. Nysteen, J. Mørk, and P. Lodahl, *Measuring the Effective Phonon Density of States of a Quantum Dot*, Phys. Rev. B **88**, 045316 (2013).

[20] M. Schatzl, F. Hackl, M. Glaser, M. Brehm, P. Rauter, A. Simbula, M. Galli, T. Fromherz, and F. Schäffler, *Local Density-of-States Mapping in Photonic Crystal Resonators by Deterministically Positioned Germanium Quantum Dots*, arXiv:1607.06701.

[21] A. Gopinath, E. Miyazono, A. Faraon, and P. W. K. Rothemund, *Engineering and Mapping Nanocavity Emission via Precision Placement of DNA Origami*, Nature (London) **535**, 401 (2016).

[22] R. Sapienza, T. Coenen, J. Renger, M. Kuttge, N. F. Van Hulst, and A. Polman, *Deep-Subwavelength Imaging of the Modal Dispersion of Light*, Nat. Mater. **11**, 781 (2012).

[23] N. Le Thomas, D. T. L. Alexander, M. Cantoni, W. Sigle, R. Houdré, and C. Hébert, *Imaging of High-Q Cavity Optical Modes by Electron Energy-Loss Microscopy*, Phys. Rev. B **87**, 155314 (2013).

[24] F. La China, F. Intonti, N. Caselli, F. Lotti, A. Vinattieri, N. Vico Triviño, J. F. Carlin, R. Butté, N. Grandjean, and M. Gurioli, *Vectorial Near-Field Imaging of a GaN Based Photonic Crystal Cavity*, Appl. Phys. Lett. **107**, 101110 (2015).

[25] N. Caselli, F. Intonti, F. La China, F. Riboli, A. Gerardino, W. Bao, A. W. Bargioni, L. Li, E. H. Linfield, F. Pagliano, A. Fiore, and M. Gurioli, *Ultra-Subwavelength Phase-Sensitive Fano-Imaging of Localized Photonic Modes*, Light Sci. Appl. **4**, e326 (2015).

[26] M. Galli, S. L. Portalupi, M. Belotti, L. C. Andreani, L. O'Faolain, and T. F. Krauss, *Light Scattering and Fano Resonances in High-Q Photonic Crystal Nanocavities*, Appl. Phys. Lett. **94**, 071101 (2009).

[27] N. Caselli, F. Intonti, F. La China, F. Biccari, F. Riboli, A. Gerardino, L. Li, E. H. Linfield, F. Pagliano, A. Fiore, and M. Gurioli, *Generalized Fano Lineshapes Reveal Exceptional Points in Photonic Molecules*, Nat. Commun. **9**, 396 (2018).

[28] N. Caselli, F. La China, W. Bao, F. Riboli, A. Gerardino, L. Li, E. H. Linfield, F. Pagliano, A. Fiore, P. J. Schuck, S. Cabrini, A. Weber-Bargioni, M. Gurioli, and F. Intonti, *Deep-Subwavelength Imaging of Both Electric and Magnetic Localized Optical Fields by Plasmonic Campanile Nanoantenna*, Sci. Rep. **5**, 9606 (2015).

[29] C. Jarlov, A. Lyasota, L. Ferrier, P. Gallo, B. Dwir, A. Rudra, and E. Kapon, *Exciton Dynamics in a Site-Controlled Quantum Dot Coupled to a Photonic Crystal Cavity*, Appl. Phys. Lett. **107**, 191101 (2015).

[30] M. Yamaguchi, T. Asano, M. Fujita, and S. Noda, *Theoretical Analysis of Light Emission from a Coupled System of a Photonic Nanocavity and a Quantum Dot*, Phys. Status Solidi C **5**, 2828 (2008).

[31] A. Lyasota, S. Borghardt, C. Jarlov, B. Dwir, P. Gallo, A. Rudra, and E. Kapon, *Integration of Multiple Site-Controlled Pyramidal Quantum Dot Systems with Photonic-Crystal Membrane Cavities*, J. Cryst. Growth **414**, 192 (2015).

[32] M. Felici, P. Gallo, A. Mohan, B. Dwir, A. Rudra, and E. Kapon, *Site-Controlled InGaAs Quantum Dots with Tunable Emission Energy*, Small **5**, 938 (2009).

[33] A. Mohan, P. Gallo, M. Felici, B. Dwir, A. Rudra, J. Faist, and E. Kapon, *Record-Low Inhomogeneous Broadening of Site-Controlled Quantum Dots for Nanophotonics*, Small **6**, 1268 (2010).

[34] A. Lyasota, C. Jarlov, P. Gallo, A. Rudra, B. Dwir, and E. Kapon, *Deterministic Coupling of a System of Multiple Quantum Dots to a Single Photonic Cavity Mode*, Appl. Phys. Lett. **111**, 053103 (2017).

[35] M. Calic, P. Gallo, M. Felici, K. A. Atlasov, B. Dwir, A. Rudra, G. Biasiol, L. Sorba, G. Tarel, V. Savona, and E. Kapon, *Phonon-Mediated Coupling of InGaAs/GaAs Quantum-Dot Excitons to Photonic Crystal Cavities*, Phys. Rev. Lett. **106**, 227402 (2011).

[36] M. Calic, C. Jarlov, P. Gallo, B. Dwir, A. Rudra, and E. Kapon, *Deterministic Radiative Coupling of Two Semiconductor Quantum Dots to the Optical Mode of a Photonic Crystal Nanocavity*, Sci. Rep. **7**, 4100 (2017).

[37] M. Feucker, R. Seguin, S. Rodt, A. Hoffmann, and D. Bimberg, *Decay Dynamics of Neutral and Charged Excitonic Complexes in Single* InAs/GaAs *Quantum Dots*, Appl. Phys. Lett. **92**, 063116 (2008).

[38] P. Lodahl, S. Mahmoodian, and S. Stobbe, *Interfacing Single Photons and Single Quantum Dots with Photonic Nanostructures*, Rev. Mod. Phys. **87**, 347 (2015).

[39] T. Yoshie, A. Scherer, J. Hendrickson, G. Khitrova, H. M. Gibbs, G. Rupper, C. Ell, O. B. Shchekin, and D. G. Deppe, *Vacuum Rabi Splitting with a Single Quantum Dot in a Photonic Crystal Nanocavity*, Nature (London) **432**, 200 (2004).

[40] M. Nomura, Y. Ota, N. Kumagai, S. Iwamoto, and Y. Arakawa, *Large Vacuum Rabi Splitting in Single Self-Assembled Quantum Dot-Nanocavity System*, Appl. Phys. Express **1**, 072102 (2008).

[41] J. P. Reithmaier, G. Sęk, A. Löffler, C. Hofmann, S. Kuhn, S. Reitzenstein, L. V. Keldysh, V. D. Kulakovskii, T. L. Reinecke, A. Forchel, G. Sek, A. Löffler, C. Hofmann, S. Kuhn, S. Reitzenstein, L. V. Keldysh, V. D. Kulakovskii, T. L. Reinecke, and A. Forchel, *Strong Coupling in a Single Quantum Dot-Semiconductor Microcavity System*, Nature (London) **432**, 197 (2004).

[42] M. Yamaguchi, A. Lyasota, and T. Yuge, *Theory of Fano Effect in Cavity Quantum Electrodynamics*, Phys. Rev. Research **3**, 013037 (2021).

[43] M. Yamaguchi, T. Asano, and S. Noda, *Photon Emission by Nanocavity-Enhanced Quantum Anti-Zeno Effect in Solid-State Cavity Quantum-Electrodynamics*, Opt. Express **16**, 18067 (2008).

[44] M. Yamaguchi, A. Lyasota, T. Yuge, and Y. Ota, *Time-Resolved Physical Spectrum in Cavity Quantum Electrodynamics*, Phys. Rev. Research **4**, 023052 (2022).

[45] A. E. Miroshnichenko, S. Flach, and Y. S. Kivshar, *Fano Resonances in Nanoscale Structures*, Rev. Mod. Phys. **82**, 2257 (2010).

[46] M. F. Limonov, M. V. Rybin, A. N. Poddubny, and Y. S. Kivshar, *Fano Resonances in Photonics*, Nat. Photonics **11**, 543 (2017).

[47] C. Jarlov, É. Wodey, A. Lyasota, M. Calic, P. Gallo, B. Dwir, A. Rudra, and E. Kapon, *Effect of Pure Dephasing and Phonon Scattering on the Coupling of Semiconductor Quantum Dots to Optical Cavities*, Phys. Rev. Lett. **117**, 076801 (2016).

[48] M. Frimmer and L. Novotny, in *Nano-Optics: Principles Enabling Basic Research and Applications*, edited by B. Di Bartolo, J. Collins, and L. Silvestri (Springer, Dordrecht, 2017), pp. 3–14.

[49] Y. Ota, R. Ohta, N. Kumagai, S. Iwamoto, and Y. Arakawa, *Vacuum Rabi Spectra of a Single Quantum Emitter*, Phys. Rev. Lett. **114**, 143603 (2015).

[50] I. V. Kulkova, A. Lyasota, C. Jarlov, B. Rigal, A. Rudra, B. Dwir, and E. Kapon, *Emission Wavelength Control of Ordered Arrays of* InGaAs/GaAs *Quantum Dots*, J. Cryst. Growth **464**, 69 (2017).

[51] A. F. Koenderink, M. Kafesaki, C. M. Soukoulis, and V. Sandoghdar, *Spontaneous Emission Rates of Dipoles in Photonic Crystal Membranes*, J. Opt. Soc. Am. B **23**, 1196 (2006).

[52] A. Delgoffe, A. Miranda, B. Rigal, A. Lyasota, A. Rudra, B. Dwir, and E. Kapon, *Tilted-Potential Photonic Crystal Cavities for Integrated Quantum Photonics*, Opt. Express **27**, 21822 (2019).

[53] D. Englund, I. Fushman, and J. Vuckovic, *General Recipe for Designing Photonic Crystal Cavities*, Opt. Express **13**, 5961 (2005).

[54] T. Reichert, S. Lichtmannecker, G. Reithmaier, M. Zeitlmair, J. Wembacher, A. Rauscher, M. Bichler, K. Muller, M. Kaniber, and J. J. Finley, *Highly Directed Emission from Self-Assembled Quantum Dots into Guided Modes in Disordered Photonic-Crystal Waveguides*, Phys. Rev. B **90**, 115310 (2014).

[55] A. Lyasota, *Interaction between Site-Controlled Quantum Dot Systems and Photonic Cavity Structures*, Ph.D. thesis, Ecole Polytechnique Fédérale de Lausanne, 2017.

[56] M. Ćalić, *Cavity Quantum Electrodynamics with Site-Controlled Pyramidal Quantum Dots in Photonic Crystal Cavities*, Ph.D. thesis, Ecole Polytechnique Fédérale de Lausanne, 2013.

[57] M. Nyman, V. Kivijärvi, A. Shevchenko, and M. Kaivola, *Generation of Light in Spatially Dispersive Materials*, Phys. Rev. A **95**, 043802 (2017).

[58] M. Nyman, A. Shevchenko, M. Kaivola, I. Shavrin, K. Lindfors, and Y. Ando, *Large-Area Enhancement of Far-Field Fluorescence Intensity Using Planar Nanostructures*, APL Photonics **4**, 076101 (2019).

[59] J. R. Johansson, P. D. Nation, and F. Nori, *QuTiP: An Open-Source Python Framework for the Dynamics of Open Quantum Systems*, Comput. Phys. Commun. **183**, 1760 (2012).

[60] U. Hohenester, *Cavity Quantum Electrodynamics with Semiconductor Quantum Dots: Role of Phonon-Assisted Cavity Feeding*, Phys. Rev. B **81**, 155303 (2010).

[61] P. Kaer, T. R. Nielsen, P. Lodahl, A. P. Jauho, and J. Mork, *Microscopic Theory of Phonon-Induced Effects on Semiconductor Quantum Dot Decay Dynamics in Cavity QED*, Phys. Rev. B **86**, 085302 (2012).

Correction: Inline equations in the last sentence of the fifth paragraph of Sec. II and in the first sentence of the third paragraph of Sec. IV have been fixed.

Second Correction: The omission of additional support information has been fixed.